Ecological Engineering 203 (2024) 107264

Contents lists available at ScienceDirect

Ecological Engineering

journal homepage: www.elsevier.com/locate/ecoleng

A Eulerian-Lagrangian model for simulating fish pathline distributions in vertical slot fishways

M.X. Ruiz-Coello [a], A. Bottacin-Busolin [a,*], A. Marion [a]

[a] *Department of Industrial Engineering, University of Padua, Italy*

ARTICLE INFO

Keywords:
Bighead carp
Silver carp
VSF
ELAM
Escaping response
CFD
Upstream migration

ABSTRACT

Recovery of the river connectivity relies on the application of structural and non-structural solutions. Within the structural solutions, vertical slot fishways (VSF) are most popular, but achieving the desired efficiency remains a challenge. To this end, evaluation of both biological and hydraulic efficiency is imperative. A Eulerian Lagrangian Agent Based Model (ELAM) of fish upstream migration through VSFs is presented in this work that considers one passive and three active behaviors affecting fish swimming pathlines of bighead carps (*Hypophthalmichthys nobilis*) and silver carps (*Hypophthalmichthys molitrix*). The passive behavior consists in a 2-D random walk where no external stimuli are detected. The first active behavior represents fish attraction to a nearby flow region as a Gaussian distribution function of turbulent kinetic energy, velocity magnitude and velocity strain rate. The second active behavior represents wall collision avoidance, whereas the third considers the tendency of the fish to escape from high velocity zones. Stochasticity is considered in the model to represent the dispersion in the experimental pathlines. The ELAM is tested for two different VSF configurations and is found to well reproduce the experimental pathlines, particularly when the escaping response to high velocity zones is considered. Results show that the ELAM model can be used as an appropriate tool for modelers and designers to evaluate fish passage efficiency.

1. Introduction

The capacity of rivers to transport sediments, organisms, nutrients, organic matter and energy is governed by their pathway connectivity. Streamflow in rivers can be highly affected by anthropogenic activity. It is estimated that 2.8 million dams are built over 500,000 km of rivers and canals worldwide (Nilsson et al., 2005). Around half of the river reaches show a diminished connectivity (Grill et al., 2019). Many fish species depend on appropriate low-energy corridors created by complex hydro-morphology conditions to complete migratory processes (McIntyre et al., 2016). Hermoso and Filipe (2021) suggest that some species are irreversibly impacted by placing a single barrier over a river reach. Fishways, usually built next to large barriers, represent a mitigation measure to maintain river connectivity rather than a solution (Silva et al., 2018). Therefore, guaranteeing their best functioning is essential in the recovering of river connectivity.

Among all types of fishway structures, Vertical Slot Fishways (VSF) are the most popular structures worldwide (Fuentes-Pérez et al., 2017) to mitigate river connectivity loss. Over 20 design configurations have been proposed (Quaranta et al., 2019; Rajaratnam et al., 1986, 1992). VSF design is focused on the control of velocities and turbulence, so that targeted fish species feel comfortable in their trajectory through the structure for both downstream and upstream migration (Larinier, 1992). Several studies have been undertaken to evaluate the hydraulic behavior and the efficiency of VSF (Baki and Azimi, 2021; Bombač et al., 2014; Fuentes-Pérez et al., 2022; Sanagiotto et al., 2019). Despite this, achieving desired passing efficiency at VSF still remains a challenge. Bunt et al. (2012) analyzed the efficiency of different fishway structures and found that VSF displayed a mean efficiency of 63% for attraction and 51% for fish passage. Noonan et al. (2012) concluded that upstream passage efficiency was around 41.7% for non-salmonid and 61.7% for salmonid fish. They also demonstrated that pool-type fishway and VSF are the most efficient fishway over other designs. Specifically, VSF displayed around 53.5% of efficiency for salmonids and 31.3% for non-salmonids. To mitigate the impact of a river barrier it is suggested a 90%–100% efficiency should be established between passing and attraction for diadromous fishes (Lucas and Baras, 2001).

Even if VSF design complies with all the hydraulic requirements

---

* Corresponding author at: Department of Industrial Engineering, University of Padua, Via Venezia 1, 35121 Padua, Italy.
E-mail address: andrea.bottacinbusolin@unipd.it (A. Bottacin-Busolin).

https://doi.org/10.1016/j.ecoleng.2024.107264
Received 23 September 2022; Received in revised form 16 April 2024; Accepted 24 April 2024

reported in the literature, fish passing efficiency might not be satisfactory. Efficiency depends not only on hydrodynamics, but also in fish swimming behavior (Castro-Santos, 2005). Therefore, addressing not only VSF hydraulic variables but also fish response is imperative in the recovery of river connectivity. In the last decades, explicit IBM models which couple ecological and biological components with hydrodynamics have been developed to model aquatic ecosystems (Willis, 2011). Goodwin et al., 2006 presented a pioneering study on this approach in which they developed and applied the Eulerian Lagrangian Agent Based (ELAM) model to reproduce the downstream migration of juvenile salmon when large barriers were placed in water bodies.

In fish swimming models, Eulerian approaches provide the information of the environment surrounding an individual, such as hydrodynamic variables and water quality indicators, essential for fish habitat selection. In addition, Lagrangian approaches track the position of individuals or groups of individuals within a computational domain. Agent Based Models represent groups of individuals which have their own set of attributes to interact with the surrounding environment and each other (DeAngelis and Grimm, 2014). In ecology, Agent Based Modelling and Individual Based Modelling (IBM) can be considered equivalent. Nonetheless, DeAngelis and Grimm (2014) characterized IBM for being able to represent local interactions, adaptive behaviors and population dynamics which cannot be represented by Partial Differential Equations (PDE). Although Goodwin and others (2006) developed their ELAM for downstream migration, their approach has also been applied to upstream path selection in VSF (Gao et al., 2016; Kulić et al., 2021; Tan et al., 2018). Particularly, Tan et al. (2018) developed an ELAM and experimentally observed juveniles Silver carps in a scaled VSF model. They found responses to hydrodynamic variables such as turbulent kinetic energy or velocity strain rate.

ELAM models have helped researchers identify different ranges of hydrodynamic variables influencing fish path selection, such as turbulent kinetic energy or velocity magnitude (Gao et al., 2016; Tan et al., 2018), as well as to optimize fishway geometry to reduce fish energy expenditure (Kulić et al., 2021). Although most of these studies have been supported by experimental data, only Kulić et al. (2021) considered fish swimming performance indicators and none included escape responses to specific flow characteristics. In fact, it has been observed that fish at barriers develop erratic swimming in presence of high velocity, pressure gradients and high turbulence intensity (Goodwin et al., 2014; Piper et al., 2015; Silva et al., 2020). It has been proven that some fish species react repulsively to some turbulent characteristics of the flow in upstream migration (Muhawenimana et al., 2019; Silva et al., 2012; Tritico and Cotel, 2010). To the best of our knowledge, the ELAM model presented in this study is the first to address a range of fish swimming capabilities, like critical swimming speed and bursting swimming speed linked to stimulus perceived by the agent. In addition, we considered an escape response to high flow velocities. To date, there is no scientific basis that a single fishway design will provide the flow conditions to target different fish species with different characteristics and swimming abilities (Silva et al., 2018).

The main purpose of this study is to evaluate the performance of an ELAM for predicting fish swimming trajectories in a Vertical Slot Fishway. The model relies on 3-D CFD simulations as inputs for an individual-based model of fish migration behavior. The IBM model is based on the experimental data of Tan et al. (2018, 2019). Four different behaviors were considered for a fish agent, assuming that the agent's behavior is only driven by hydrodynamic variables. Variability due to external stimuli such as light or temperature, or due to internal stimuli such as stress or fatigue are addressed by adding some stochasticity in path and swimming speed selection. Some other assumptions were considered. First, the agent's swimming direction is mainly counter current. Second, energy expenditure is evaluated, although disregarded in the ELAM. Third, an efficiency of 100% is assumed, i.e. all agents in the simulations will succeed at passing the VSF. As a secondary objective, we aim to analyze the influence of each hydrodynamic variable on path selection and to evaluate the distribution of pathlines described by fish. Finally, we assess the effect of an escape response to high flow velocities and its effect on the agent's energy consumption through the fishway.

2. Materials and methods

2.1. Experimental data

Tan and others (2019, 2018) performed a series of experiments in a 1:2.5 scale physical model built at the Engineering Research Center of Eco-Environment in Three Gorges reservoir region, Yichang (China). The hydrodynamic channel was 7.0 m (L) long and 0.5 m (B) wide. Experiments were conducted in 5 pools, each 0.625 m (Lp) long. The opposite baffles, having a length of 0.25 m (= b1) and 0.125 m (= b2), were staggeringly arranged in opposite sides on the for the first two treatments sidewall (C1.1 & C1.2, Tan et al., 2019) and in the same side of the sidewall for the third (C2, Tan et al., 2018). The slope of the channel in both cases was 1%, the inlet was located 2.375 m upstream of the first baffle and the outlet 1.25 m downstream of the last baffle. They tested 15 individuals of the bighead carp (*Hypophthalmichthys nobilis*) with 18 l/s of flow rate for C1.1, 18 individuals with 26 l/s of flow rate for C1.2 and 30 individuals of the silver carp (*Hypophthalmichthys molitrix*) for C2. Configurations C1 and C2 are shown in Fig. 1. A summary of the characteristics of each case is presented in Table 1.

Albeit the experiments were performed with different fish species, i.e. bighead carp and silver carp (Table 1), we consider Asian carp as the reference species for all cases in light of the availability of experimental data. Asian carps are endemic from eastern Asia, but have been introduced in the Americas, Europe and throughout Asia. They are usually found in turbid water such as the Yangtze River in China or the Mississippi River in the in the US, where they are considered injurious species (Nico et al., 2023a, 2023b). Asian carps studies have been widely developed both in endemic (Fang et al., 2022; Feng et al., 2019; Tan et al., 2018, 2019, 2022) and nonnative ecosystems (George and Chapman, 2013; Hoover et al., 2017). They tend to choose habitats with relatively calm waters, rich biological bait and low human interventions (Fang et al., 2019). Both bighead and silver carps are fresh water cyprinid fish, which exhibit regular migratory habits for spawning and nursery periods, between lakes and rivers (Lucas and Baras, 2001).

2.2. Hydrodynamic model – Eulerian framework

We performed a 3-D CFD simulation (Eulerian) for each geometry using the CFD code OpenFOAM v2112 (ESI Group, 2022). For all the cases, we solved the incompressible Reynolds Averaged Navier-Stokes (RANS) Equations:

$$\frac{\partial \overline{u}_i}{\partial x_i} = 0 \tag{1}$$

$$\frac{\partial \overline{u}_i}{\partial t} + \overline{u}_j \frac{\partial \overline{u}_i}{\partial x_j} = -\frac{1}{\rho}\frac{\partial \overline{p}}{\partial x_i} + \frac{\partial}{\partial x_j}\left[(\nu+\nu_t)\left(\frac{\partial \overline{u}_i}{\partial x_j} + \frac{\partial \overline{u}_j}{\partial x_i}\right) - \frac{2}{3}\delta_{ij}k\right] + \mathrm{f}_i \tag{2}$$

where x is the space, t is time, $\overline{u}$ is the averaged velocity, ρ is fluid density $\overline{p}$ is the averaged pressure, ν is the kinematic viscosity of the fluid, ν_t is the turbulent kinematic viscosity, δ_{ij} Is the Kroneker delta, k is the turbulent kinetic energy (TKE) and, f is the body force, $i.j = 1,2,3$. ν_t is computed through turbulence modelling. Validated simulation results in VSF have been published with regards to the standard k-ε (An et al., 2016; Baharvand and Lashkar-Ara, 2021; Fuentes-Pérez et al., 2017) and RNG k-ε (Stamou et al., 2018; Tan et al., 2019) models. In this study, simulations were performed using the RNG k-ε turbulence model:

$$\nu_t = C_\mu \frac{k^2}{\varepsilon} \tag{3}$$

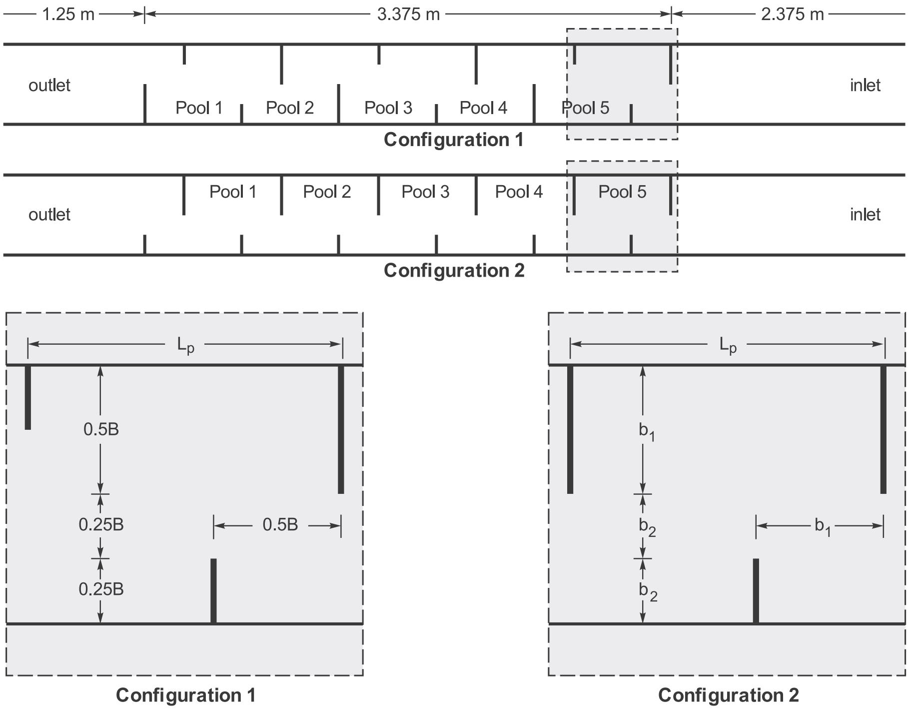

Fig. 1. Geometry and dimensions of the vertical slot fishway.

Table 1
Summary of the case studies extracted from Tan et al. (2018, 2019). In the table, n is number of individuals and Q is discharge.

Case	Fish species	n	VSF configuration	Q (l/s)
C1.1	Bighead carp	15	Baffles staggeringly arranged	18
C1.2	Bighead carp	18	Baffles staggeringly arranged	26
C2	Silver carp	30	Baffles uniformly arranged	13

$$\frac{\partial k}{\partial t}+\overline{u}_j\frac{\partial k}{\partial x_j}=\frac{\partial}{\partial x_j}\left[\left(\nu+\frac{\nu_t}{\sigma_k}\right)\frac{\partial k}{\partial x_j}\right]+G-\varepsilon \tag{4}$$

$$\frac{\partial \varepsilon}{\partial t}+\overline{u}_j\frac{\partial \varepsilon}{\partial x_j}=\frac{\partial}{\partial x_j}\left[\left(\nu+\frac{\nu_t}{\sigma_\varepsilon}\right)\frac{\partial \varepsilon}{\partial x_j}\right]+C_{\varepsilon 1}\frac{\varepsilon}{k}G-C_{\varepsilon 2}\frac{\varepsilon^2}{k}-C_\mu\eta^3\frac{1-\eta/\eta_0}{1+\beta\eta^3}\frac{\varepsilon^2}{k} \tag{5}$$

$$G=\nu_t\left(\frac{\partial \overline{u}_i}{\partial x_j}+\frac{\partial \overline{u}_j}{\partial x_i}\right)\frac{\partial \overline{u}_i}{\partial x_j} \tag{6}$$

where $\eta = (k/\varepsilon)(G/\nu_t)^{0.5}$, β is 0.012 and η_0 is 4.38, C_μ, $C_{\varepsilon 1}$, $C_{\varepsilon 2}$, σ_k and σ_ε are empirical coefficients whose values are 0.085, 1.42, 1.68, 0.7194 and 0.7194, respectively. Considering the multiphase nature of the phenomenon, we used the *interFoam* solver, which has been proven suitable for simulation of sharp continuous interfaces in open channel flows (Fuentes-Pérez et al., 2018; Jiang et al., 2018)**.** ***interFoam*** solves multiphase flow (2 immiscible fluids) using the PIMPLE algorithm and hydrostatic pressure contributions (ESI Group, 2022). The solver implements Volume of Fluid (VoF) method (Hirt and Nichols, 1981) to track the free surface interphase in open channel flows:

$$\frac{\partial \alpha}{\partial t}+\frac{\partial(\overline{u}_i\alpha)}{\partial x_i}=0 \tag{7}$$

where, α is the fluid fraction (0–1), generally of the denser fluid. All variables in each cell volume, ξ, are averaged at the interface:

$$\xi=\xi_{water}\alpha+\xi_{air}(1-\alpha) \tag{8}$$

The grid was structured with refinement at the baffles. Mean cell size was 0.02 m and the number of cells was approximately 550,000 elements for each model. Time step was dynamically computed considering a maximum courant number of CFL = 0.45 for stability. Mesh configuration is displayed in Fig. 2.

We defined three open boundaries, i.e. inlet, outlet, and atmosphere, and wall boundaries on the channel walls, respectively. The wall type boundary condition was defined as no slip condition. The domain was split in two blocks, to control the water depth at the inlet boundary in which the inflow rate was defined. In contrast, the mean water flow velocity was set in the outlet condition to keep the downstream water level. Boundary conditions for the CFD simulation (Eulerian) are presented in Table 2.

Previous studies have shown that the bed friction coefficient has little influence on the flow dynamics of the fishway for both 2D (Bombač et al., 2014; Cea et al., 2007) and 3D numerical models (Barton and Keller, 2003). Therefore, roughness was neglected in the simulation. Once initialized, the simulation time for each simulation was 200 s, which ensured the achievement of a steady state condition and satisfaction of the continuity equation (i.e., $Q_{in} \approx Q_{out}$, where Q_{in} is the discharge at the inlet and Q_{out} is the discharge at the outlet). The resolution of the computational grid used in this study is consistent with the findings of Ruiz-Coello et al. (2024), who performed a grid convergence analysis using the same 3D model used in this study.

2.3. *Lagrangian framework and sensorial system*

In habitat modelling, Eulerian models are able to represent physical (hydrodynamics) and chemical (water quality/heat transfer) variables, while Lagrangian models predict the particle positions within the Eulerian model domain (Baharvand et al., 2023; Nestler et al., 2016; Periáñez, 2020). In our model we use one-way Eulerian-Lagrangian coupling, according to which the hydrodynamic variables influence fish motion, but fish motion does not influence the hydrodynamic variables. In the Lagrangian fish model, the motion of a fish satisfies the equation:

$$\frac{\partial x_{Pi}}{\partial t}=u_{fish,i} \tag{9}$$

where $x_{P,i}$, $i = 1,2,3$, is the position along the x_i axis, and $u_{fish,i}$ is the

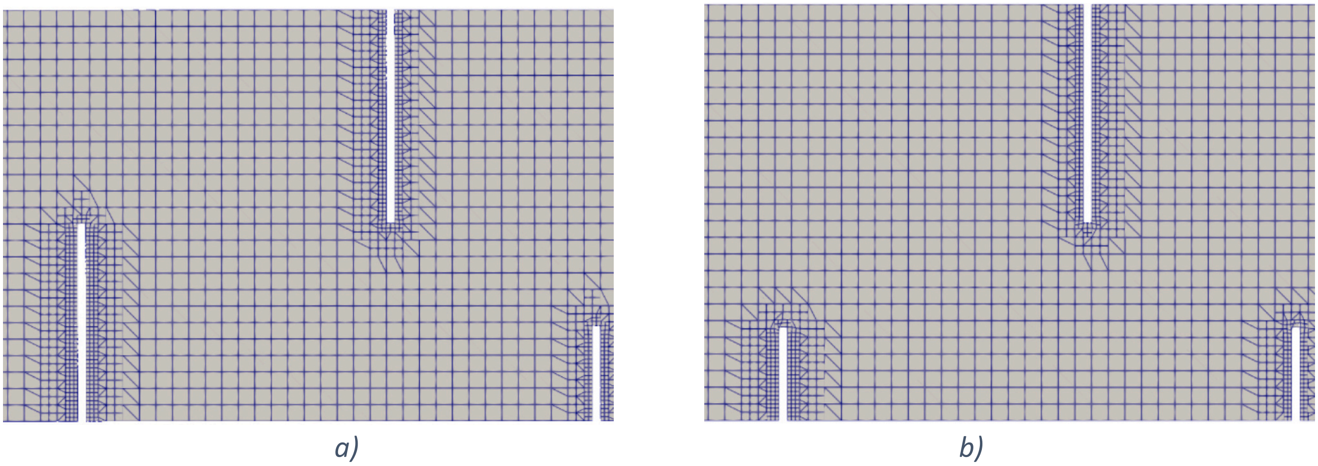
a)
b)

Fig. 2. Computational mesh on the x-y plane used in the flow simulations a) Configuration C1; b) Configuration C2.

Table 2
CFD model boundary conditions according to the OpenFOAM nomenclature.

Variable	inlet	outlet	walls	atmosphere
p_{hyd}	*zeroGradient*	*zeroGradient*	*fixedFluxPressure*	*totalPressure*
$\overline{u}_i$	*variableHeightFlowRateInletVelocity*	*outletPhaseMeanVelocity*	*noSlip*	*pressureInletOutletVelocity*
k	*fixedValue*	*inletOutlet*	*kqRWallFunction*	*inletOutlet*
ε	*fixedValue*	*inletOutlet*	*epsilonWallFunction*	*inletOutlet*
α	*variableHeightFlowRate*	*zeroGradient*	*zeroGradient*	*inletOutlet*

agent's velocity determined by different hydrodynamic stimuli according to a behavioral model.

Fish use lateral line system to sense changes in the fluid flow environment. The fish lateral line is composed of superficial neuromast (SNs), which filters hydrodynamic stimuli, and canal neuromasts (CNs), which measures free stream acceleration by processing pressure gradients on the fish surface (van Netten and McHenry, 2014). Using the lateral line system, fish can sense hydrodynamic variables such as velocity, acceleration, pressure gradients and shear stress. Goodwin et al. (2006) called their model Numerical Fish Surrogate (NFS) approach, which scales fish sensorial perception by defining a symmetrical sensory ovoid constrained by a Sensory Query Distance (SQD). In order to reproduce the lateral line sensorial system, we followed the NFS approach. However, we adopted Gao et al.'s (2016) proposal, which assumes that the sensory query distance is a function of the Body Length, BL, and a random variable, RN:

$$SQD = max(\Delta x_i, BL \bullet (1 + 0.5 \bullet RN)) \tag{10}$$

in which RN is randomly generated at each time step between 0 and 1. According to eq. (10), SQD should not be larger than 1.5BL, where BL was randomly chosen for each simulation between 0.1 and 0.15 m. Asian carps swimming performance indicators were taken from Cai et al. (2020), who conducted a study on swimming performance parameters linked to BL for six different carp species along a VSF in China. They concluded that the critical swimming speed, U_{crit}, which is the maximum sustained swimming speed (aerobic swimming capability) that the fish can sustain over 200 min without fatigue (Hammer, 1995), is 2.62–9.23 BL/s; and the burst swimming speed, U_{burst}, i.e. the highest speed that the fish can reach for escaping maneuvers shorter than 15 s (Hammer, 1995), is 3.35–9.38 BL/s with BL in meters. The results presented by Cai et al. (2020) are in contrast with those found earlier by Newbold et al. (2016), who found that the mean U_{crit}, 3.84 BL/s, was approximately the half of mean U_{burst}, 7.80 BL/s, for the bighead carp. In addition, similarly to Cai et al. (2020), they observed that high individual variation in swimming speed produced an overlap between the ranges of prolonged and burst swimming speed. Thus, we used the mean U_{crit} presented by Newbold et al. (2016) as the highest value in our model. These values randomly change, with a uniform distribution, at each time step within the range specified.

The experimental data are from juveniles, which can be 0.1–0.15 m in length. However, previous studies have shown that while the absolute swimming speed is smaller in juveniles, the relative swimming speed can reach up to 15 BL/s (Hoover et al., 2017; Tan et al., 2021). The ranges selected in this study belong to adults and should provide a general model for Asian carps. It is important to note that the chosen swimming performance indicators do not reach the maximum values observed for juveniles but fall within the range of their typical swimming performance. In addition, the hydraulics of the VSF evaluated by Tan et al. (2018, 2019) are somewhat unconventional and relatively calm, with no challenging water drops, so that the carps do not need to use their maximum swimming performance.

2.4. Individual based model

Neurophysiological recordings of superficial neuromast (SNs) are velocity sensitive at frequencies below 50 Hz (McHenry and Liao, 2014). However, canal neuromasts (CNs) sensorial frequency can go up to 200 Hz. Indeed, the canal neuromasts (CNs) display a superior response to flow velocities at frequencies over 10 Hz (van Netten and McHenry, 2014). Considering this evidence, the time step in which the agent screens the environment and chooses the most suitable path should be between 0.02 and 0.1 s. The agent's time step, Δt_{fish}, was therefore set to 0.05 s to guarantee a proper time discretization of the fish line paths and not to be in the edge of the frequency ranges. To determine the impact of the time step in the IBM predictions, an additional study was performed within the ranges of frequencies of the sensorial responses. The results are presented in the supplementary information and confirm the selection of $\Delta t_{fish} = 0.05\ s$ as the most suitable time step.

Considering that VSF hydraulics is mainly two-dimensional (Bombač et al., 2014), the IBM model is designed to work in a 2D quasi-steady state flow field, in which the inflow remains approximately equal to the outflow throughout the simulation. The flow field is taken as the *xy* plane at a height of z/h = 0.6 of the 3-D simulations described in section 2.2. Stimuli, actions, and conditions of each behavior are summarized in Table 3. Contrary to (Tan et al., 2018), the Eulerian input in this case is not the 2-D depth-averaged hydraulics, but the selected *xy* plane at z/h = 0.6 can be taken as most representative of the depth-averaged flow variables. Finally, based on the results published by Ruiz-Coello et al. (2024) and the fact the results are extracted by interpolation at z/h = 0.6, the resolution of the computational mesh is not likely to impact on the agent's response.

IBMs are models which describe populations as ensembles of individuals with their own set of attributes which determine the interactions with the surrounding environment and with each other (DeAngelis and Grimm, 2014). The model presented in this work follows the general approach proposed by Goodwin et al. (2006), in which the Eulerian domain is the surrounding environment, local interactions are addressed by the Lagrangian model (eq. 9), the sensorial system and the adaptative behavior is described by the IBM. Fig. 3 shows the four behaviors described in Table 3.

2.4.1. *Behavior 0: Random Walk*

Random walk behavior, B_0, is triggered when there is no cell suitable enough within the SQD sphere such that $P_i \leq P_{threshold}$, where the probability $P_{threshold}$ was set to 0.05. This implies that the agent will select this behavior in quasi-still water state. It is coded as Correlated Random Walk (CRW), whereby the displacement of the agent is correlated with the previous agent's state (Codling et al., 2008). Specifically, the agent only updates its swimming direction with a uniformly random change of direction between -30° and 30° (ϕ) (Fig. 3a). Fish velocity is given by:

$$\overrightarrow{u}_{fish} = U_{crit} \bullet \left(\frac{\overrightarrow{u}_{fish}}{\left|\overrightarrow{u}_{fish}\right|} \right|_{\theta=\theta+\phi} \left. \vphantom{\frac{\overrightarrow{u}}{\overrightarrow{u}}} \right) \tag{11}$$

where $\overrightarrow{u}_{fish}$ is the agent's velocity and θ is the angle of $\overrightarrow{u}_{fish}$ respect to the *x*-axis.

2.4.2. *Behavior 1: Attraction towards the most suitable cell*

Decision making is based on two components, information processing and response generation. Internal responses in fish decision making can be represented by a dual Gaussian distribution of noise alone and stimulus plus noise (Kemp et al., 2012). Following Tan et al. (2018), we assumed a single Gaussian Probability Density Function (PDF) for this behavior, B_1. The stimuli triggering a response are turbulent kinetic energy (TKE), velocity magnitude (U) and velocity strain rate (SR). Since each variable have different units, the PDF for Behavior 1 was normalized by the peak probability:

$$p(\Phi_j) = \left(\frac{1}{\sigma\sqrt{2\pi}} e^{-\frac{1}{2}\left(\frac{\Phi_j-\mu}{\sigma}\right)^2} \right) \Big/ p(\Phi_j)_{Peak} \tag{12}$$

$$P_i = \sum_{j=1}^{3} W_j \bullet p(\Phi_j) \tag{13}$$

where Φ_j is the hydrodynamic variable, μ is the fish preferred value (mean) of the hydrodynamic variable, σ is its variability, $p(\Phi_j)$ is the normalized PDF (0–1), p_{peak} is the peak value of the distribution, P_i is the joint probability from the cells within the SQD sphere, and W_j is the weight of each variable (TKE, U & SR) in the joint probability. μ and σ were found through the statistics of the spatial dispersion from experimental data (Tan et al., 2018, 2019) over the CFD simulation results, while W_j is tuned through the calibration and validation process. The agent's velocity is given by:

$$\overrightarrow{u}_{fish} = U_{crit} \bullet \frac{\overrightarrow{D}}{\left|\overrightarrow{D}\right|} \tag{14}$$

where $\overrightarrow{D}$ is the distance vector between agent's position and the selected cell. This behavior follows Tan et al.'s (2018) model. However, in our model, the agent samples all the cells and chooses randomly among the 50% most suitable cells in the SQD sphere in the upstream direction. Railsback and Grimm (2012) suggest adding random noise or a consistent bias to how the agent processes information. In this sense, stochasticity is used also to address the variability of complex processes that are not considered in this formulation. In our study, only hydrodynamic stimuli are considered to drive agent's behavior, thus neglecting all other internal and external stimuli.

Table 3
Agent's behavior criteria implemented in the Individual Based Model (IBM).

Behavior	Stimulus	Action	*Condition
0	none	Random walk	$P_i \leq P_{threshold}$
1	Hydrodynamic variables	Attraction	$P_i > P_{threshold}$
2	Wall boundary	Avoidance	$\left\|\overrightarrow{U}_i\right\| = 0$
3	High velocity flow fields	Escape response	$\left\|\overrightarrow{U}_i\right\| \geq U_{threshold}$

[*] P_i: Joint probability (likelihood of choosing a path), $P_{threshold}$: Threshold value of P_i, $\overrightarrow{U}_i$: Flow velocity, $U_{threshold}$: Threshold value of $\left|\overrightarrow{U}_{i.}\right|$

2.4.3. *Behavior 2: Wall avoidance*

Although the main fish sensory input may be visual (Montgomery et al., 2000), they use their mechanosensory lateral line system to sense changes in flow field characteristics generated by obstacles to avoid collision (Windsor et al., 2008, 2010). Consistently with this fact, Behavior 2, B_2, is triggered when a cell with zero velocity magnitude, $|U_i| = 0$, is found in the half inner radius of the SQD sphere. This velocity magnitude is found in near-wall regions, as the no slip condition is imposed on the walls (Table 2). According to this type of behavior, a velocity in the direction opposite to the sidewalls towards the jet region is added to the velocity defined in Behavior 1 according to a weighted average:

$$\overrightarrow{u}_{fish} = U_{crit} \bullet \left(RW \bullet \frac{\overrightarrow{D_1}}{\left|\overrightarrow{D_1}\right|} + (1 - RW) \bullet \frac{\overrightarrow{D_2}}{\left|\overrightarrow{D_2}\right|} \right) \tag{15}$$

in which $\overrightarrow{D_1}$ is the distance vector between agent's position and the most suitable cell, $\overrightarrow{D_2}$ is the distance vector between agent's position and the closest cell at the jet region at baffle's position. *RW* is a random variable that varies at each time step between 0.05 and 0.5. Moreover, the agent can identify sidewalls (parallel to main agent's swimming direction) and baffles (perpendicular to main agent's swimming direction). When the agent finds a wall baffle, the condition constrains the SQD sphere, allowing the agent to choose among all suitable cells behind the baffle (Fig. 3c).

2.4.4. *Behavior 3: Escape from high velocity regions*

Piper et al. (2015) observed that European Eels (*Anguilla anguilla*) displayed an escaping behavior when exposed to high velocity gradients. Silva et al. (2020) also observed that rapid swimming, at speeds even higher than estimated U_{burst}, of smolts of Atlantic salmon (*Salmo salar*) occurred in zones with high gradients of velocity magnitude and direction and where TKE was highest.

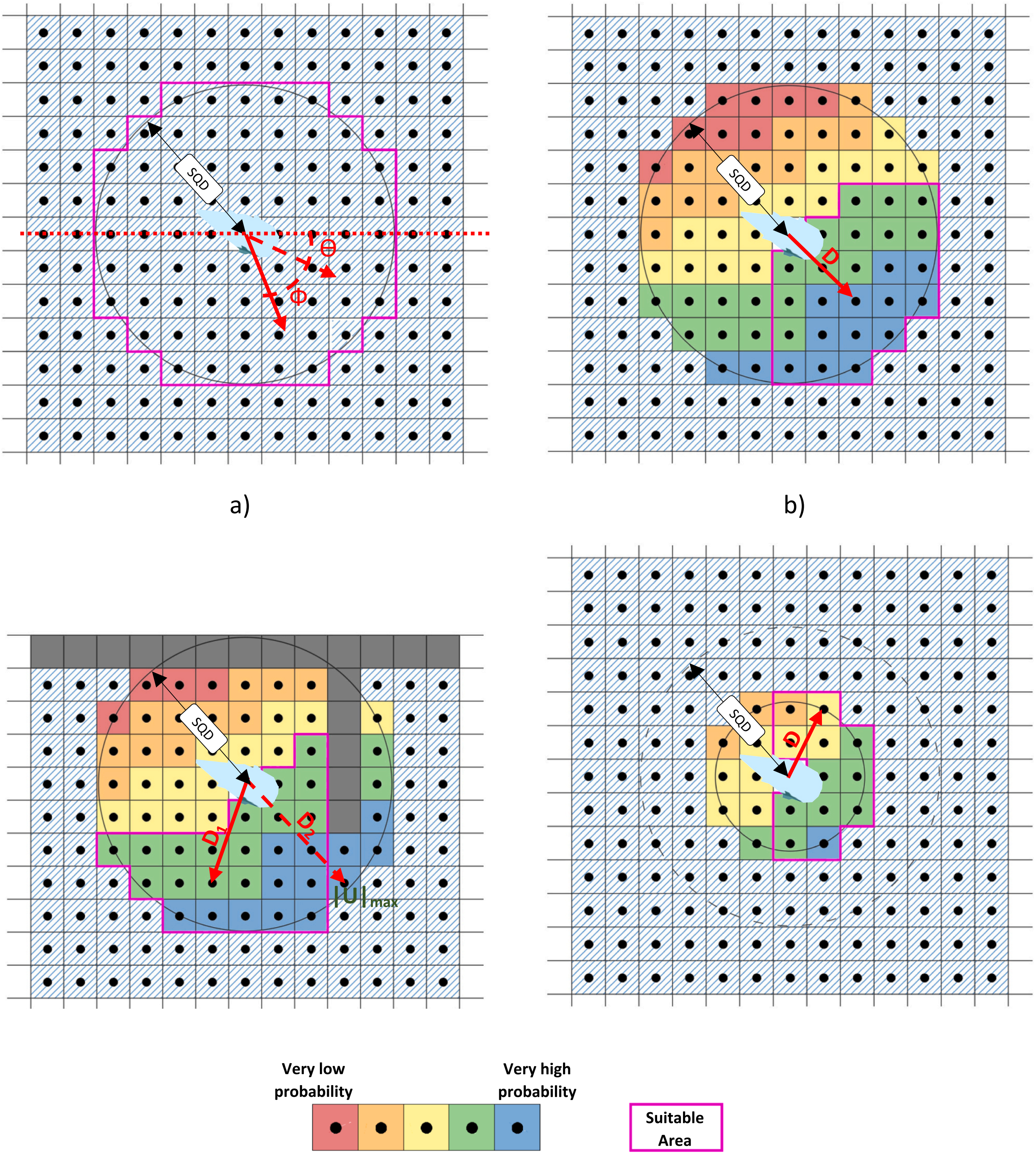

Fig. 3. Illustration of the sensory query circle and cell selection probabilities for the different behaviors; a) Behavior 0; b) Behavior 1; c) Behavior 2; d) Behavior 3.

Behavior 3, B_3, represents a deviation from the default fish behavior. Although the agent's swimming direction follows the same rules described for Behavior 1, when flow velocity magnitudes within the SQD sphere are higher than $U_{threshold} = \mu_U + 1.75 \bullet \sigma_U$ an alternative behavior governs the agent, which considers the effect of uncomfortable velocities. First, the uncertainty in the selection of the most suitable cells defined in Behavior 1 increases from 50% to 75% of most suitable cells. Second, the SQD sphere radius is reduced by half, constraining the agent sensory scope (Fig. 3c). Finally, the agent uses U_{burst} instead of U_{crit} as velocity magnitude. This behavior aims to replicate the fish escaping response when it experiences high accelerated flows.

2.5. Calibration and validation

Model validation is based on the experimental data published by Tan et al. (2018, 2019). After extracting from their datasets, the trajectories described by the fish within the fishway, a polynomial regression model of order 10 was applied to the data to define the average trajectory of the fish. We then defined the Root Mean Square Error (RMSE) between the simulated trajectory and average trajectory as an objective function for model calibration. For each case, 1000 simulations were performed for different values of the coefficient W_j in eq. 13. After finding the coefficients minimizing the RMSE and considering the dispersion in the experimental data, 15, 18 and 30 agents were simulated for C1.1, C1.2 and C2, respectively, to replicate the experimental data. The y-axis variability in the simulated fish pathlines was compared with the experimental data by using the mean pathline obtained by polynomial regression and the first two central moments (mean, μ_y, and standard deviation, σ_y) evaluated at 30 spatial intervals in the transverse sections. In each configuration, experimental data is available for pools 2, 3 and 4. A linear regression model between simulated and observed carps positions (Correndo et al., 2021; Smith and Rose, 1995) for both the polynomial function and the mean paths, μ_y, (eq. 16) was applied to evaluate the goodness of fit of the model:

$$Y_i = a + mX_i \tag{16}$$

where Y_i are the observed data values, X_i are the simulated values, a is intercept and m is the slope of the regression function. The null hypothesis corresponds to $a = 0$ and $m = 1$. A metric of the correlation between Y_i and X_i is given by the coefficient of determination, R^2 (Yang et al., 2014), Moreover, the dispersion of the pathlines along the y-axis was evaluated globally rather than at each interval. Comparison with the average pathline and the mean transverse position μ_y must be complemented by the evaluation of the dispersion around the mean pathline, σ_y, to ensure that the ELAM provides a suitable statistical description of the trajectory described by the fish.

2.6. Energy cost assessment

Energy cost was evaluated by calculating the drag power, which represents the energy loss per unit time (Fish, 2010):

$$\frac{\Delta E}{\Delta t} = \frac{1}{2} \bullet \rho \bullet S \bullet C_D \bullet {U_P}^3 \tag{17}$$

where ΔE is work done by the agent, Δt is the time step, S is the wetted area, i.e. an ellipsoid of revolution with dimensions BL, 0.5BL and 0.25BL, $C_D = 0.015$ is the drag coefficient (Webb, 1975), and U_P is

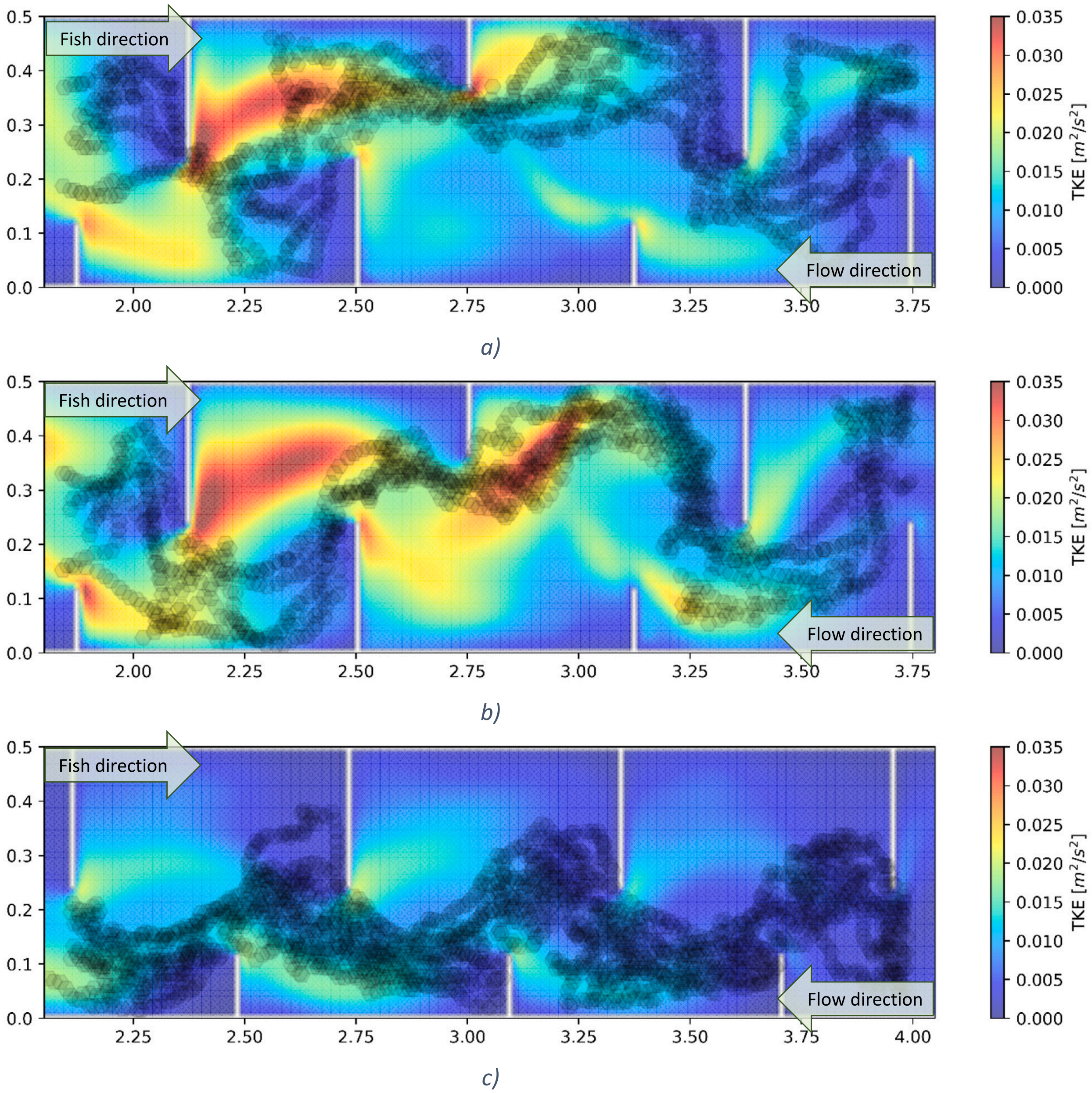

Fig. 4. Turbulent kinetic energy, TKE, at z/h = 0.6 and experimental distribution of migration pathlines (Tan et al., 2018, 2019); a) case C1.1; b) case C1.2; c) case C2.

the agents relative velocity magnitude given by $U_P = \left|\overrightarrow{u}_{fish} - \overrightarrow{U}\right|$. Kulić et al. (2021) used a similar approach to assess fish energy consumption. Although, in practice, the drag coefficient is far from being constant, there are no empirical relationships that link the drag coefficient of a fish to the Reynolds number, therefore the value assumed should be interpreted as a reference value corresponding to typical fish swimming speeds. This may lead to errors in the evaluation of the energy consumption in low velocity zones, but since energy consumption scales with $U_P{}^3$, we expect their contribution to the overall energy consumption to be relatively small.

3. Results

3.1. Hydrodynamic model

The hydrodynamic simulations converged to steady state in around 150 s of simulation time. Fig. 4, Fig. 5 and Fig. 6 display the spatial distribution of the hydrodynamic variables (TKE, U, SR) on the *xy* plane (z/h = 0.6) at time $t = 200$ s, which ensured steady state conditions in all simulations. The black circles represent the positions occupied by the Asian carps as they migrate upstream along the fishway in the experimental work of Tan et al. (2018, 2019).

The maximum TKE values found in the simulations were 0.039, 0.046 and 0.028, m^2/s^2, while the maximum values of the velocity magnitude, *U*, were 0.77, 0.81, and 0.65 m/s, for C1.1, C1.2, C2, respectively. The maximum SR value was set to 10 s^{-1} so that zones with SR greater than the maximum are considered highly variable. Within the zones SR $\leq$ 10 s^{-1}, mean values of SR were 3.32, 3.48, and 3.53 s^{-1}, for C1.1, C1.2, C2, respectively. Mean values of SR are not very different. Therefore, the analysis focuses on the zones characterized by high velocity gradients (SR > 10 s^{-1}).

As in Tan et al. (2018, 2019), the hydrodynamic variables of the VSF where extracted from the pools 2, 3 and 4 at the plane *xy*, $z/h = 0.6$, for further analysis. The hydrodynamics of C1.1 and C1.2 are similar, with mean TKE in the domain equal to 0.008 and 0.010 m^2/s^2, respectively.

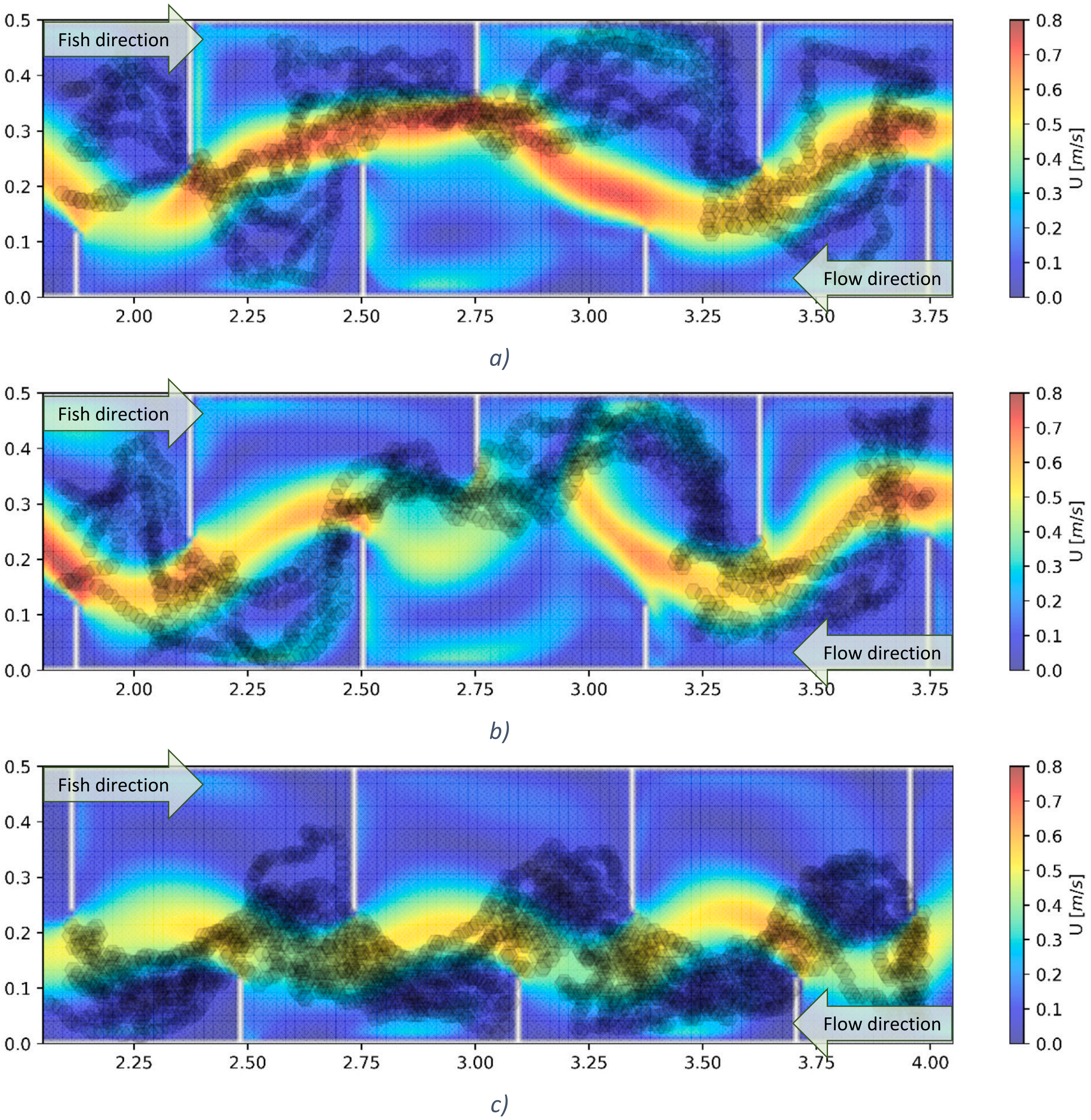

Fig. 5. Velocity magnitude, U, at z/h = 0.6 and experimental distribution of migration pathlines (Tan et al., 2018, 2019); a) case C1.1; b) case C1.2; c) case C2.

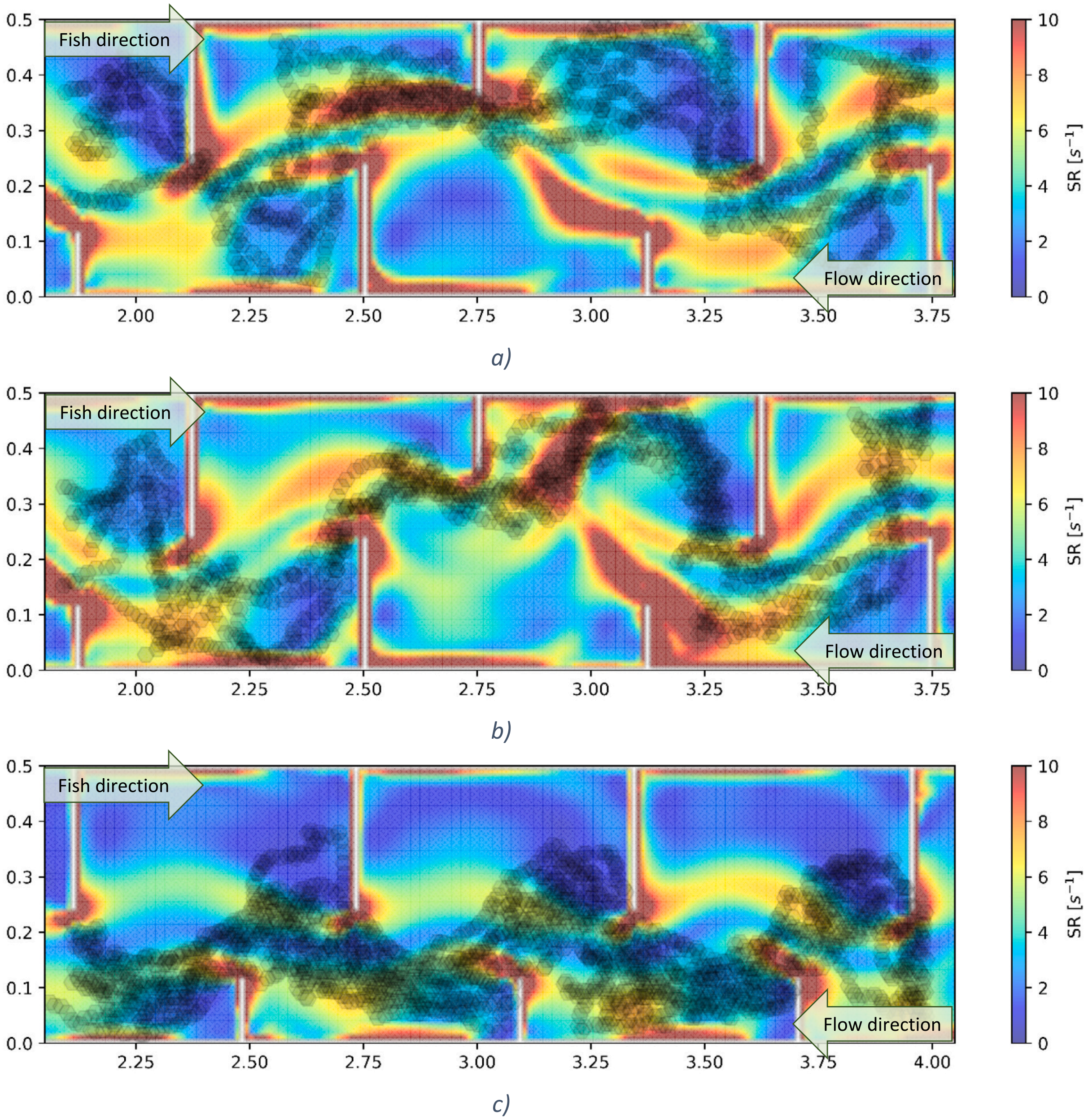

Fig. 6. Strain rate, SR, at z/h = 0.6 and experimental distribution of migration pathlines (Tan et al., 2018, 2019); a) case C1.1; b) case C1.2; c) case C2.

67.86% and 57.74% of the selected domains display values lower than 0.01 m^2/s^2, as well as 90.80% and 85.96% lower than 0.02 m^2/s^2, respectively. The mean velocity U is 0.15 and 0.19 m/s, respectively. However, this value increases up to 0.20 and 0.24 m/s for C1.1 and C1.2, respectively, in the part of the domain for which $y \in [0.1, 0.4]$ where the maximum velocities are found. In 73.62% and 71.77% of the domain, the velocity U is lower than the mean value. Finally, 55.13% and 65.97% of the domain displays strain rates lower than 10 s^{-1} for C1.1 and C1.2, respectively.

For the C2 geometry, turbulence intensity is significantly different. The mean value of TKE is 0.004 m^2/s^2, which is half of the value found for C1.1 and C1.2. Moreover, in 87.54% of the selected domain TKE values are below 0.01 m^2/s^2. C2 is significantly less turbulent than C1.1 and C1.2. On the other hand, the mean velocity magnitude in the whole domain is 0.11 m/s and 0.19 m/s for $y \in [0.1, 0.3]$, where the slot openings and maximum velocities are located. These values are not significantly different compared to those in the C1.1 and C1.2 configurations. In C2, 84.52% of the total domain is characterized by velocities lower than the mean for $y \in [0.1, 0.3]$. Finally, 66.50% of the total domain displays SR values lower than 10 s^{-1}.

Maximum velocities are 0.81, 0.87 and 0.63 m/s and water depth of 0.24, 0.34 and 0.26 m for C1.1, C1.2 and C2, respectively. The highest Froude numbers are 0.56, 0.48, and 0.40, respectively, so all the configurations are in the subcritical regime even in the jet region. Consistently with this fact, water drops are not pronounced and there are no step changes in the free surface elevation along the VSFs.

3.2. ELAM calibration and validation

The Eulerian CFD simulations were followed by statistical analysis and model validation. The preferred values for upstream carp migration (μ_j) are 0.08–0.012 m^2/s^2 for TKE, 0.25–0.29 m/s for U and 4.24–5.15 s^{-1} for SR. After a sensitivity analysis, the weighting W_j of the hydrodynamic variables according to eq. (13) in the C1 case was 0.82–0.86 for TKE, 0.09–0.13 for U and 0–0.08 for SR. Table 4 shows the calibrated coefficients (attraction behavior, B_1).

Table 4
Calibrated coefficients for attraction behavior, B_1.

Case	Q (l/s)	TKE			U			SR		
		μ (m^2/s^2)	σ (m^2/s^2)	W (−)	μ (m/s)	σ (m/s)	W (−)	μ (1/s)	σ (1/s)	W (−)
C1.1	18.0	0.0121	0.0064	0.860	0.287	0.215	0.138	5.147	1.121	0.002
C1.2	26.0	0.0120	0.0058	0.824	0.264	0.166	0.091	4.813	2.911	0.085
C2	13.5	0.0083	0.0038	0.741	0.250	0.165	0.101	4.239	2.963	0.159

The agents' trajectories were verified with the validation tests described in section 2.5. Validation coefficients a, m and R^2(eq. 16) before including Behavior 3 are displayed in Fig. 7a and Fig. 7b, and in Fig. 7c and Fig. 7d after including Behavior 3. The first two figures show the polynomial regression, $y_{path} = f(x)$, and the first statistic moment of the agent's position along the y-axis, μ_y.

Summarizing the results of the validation based on pathline regression, y_{path}, the coefficients a, m and R^2 before including the escape response, B_3, are in the ranges of [−0.11, 0.04], [0.99, 1.55], and [0.52, 0.68], respectively. After including it, they are found within the ranges [−0.12, −0.03], [1.25, 1.6], and [0.68, 0.86], respectively. These results show that the performance of the model was improved by adding the escape response, B_3. For the validation based on the first statistical moment, μ_y (m), the coefficients a, m and R^2 are in the ranges of [−0.08,

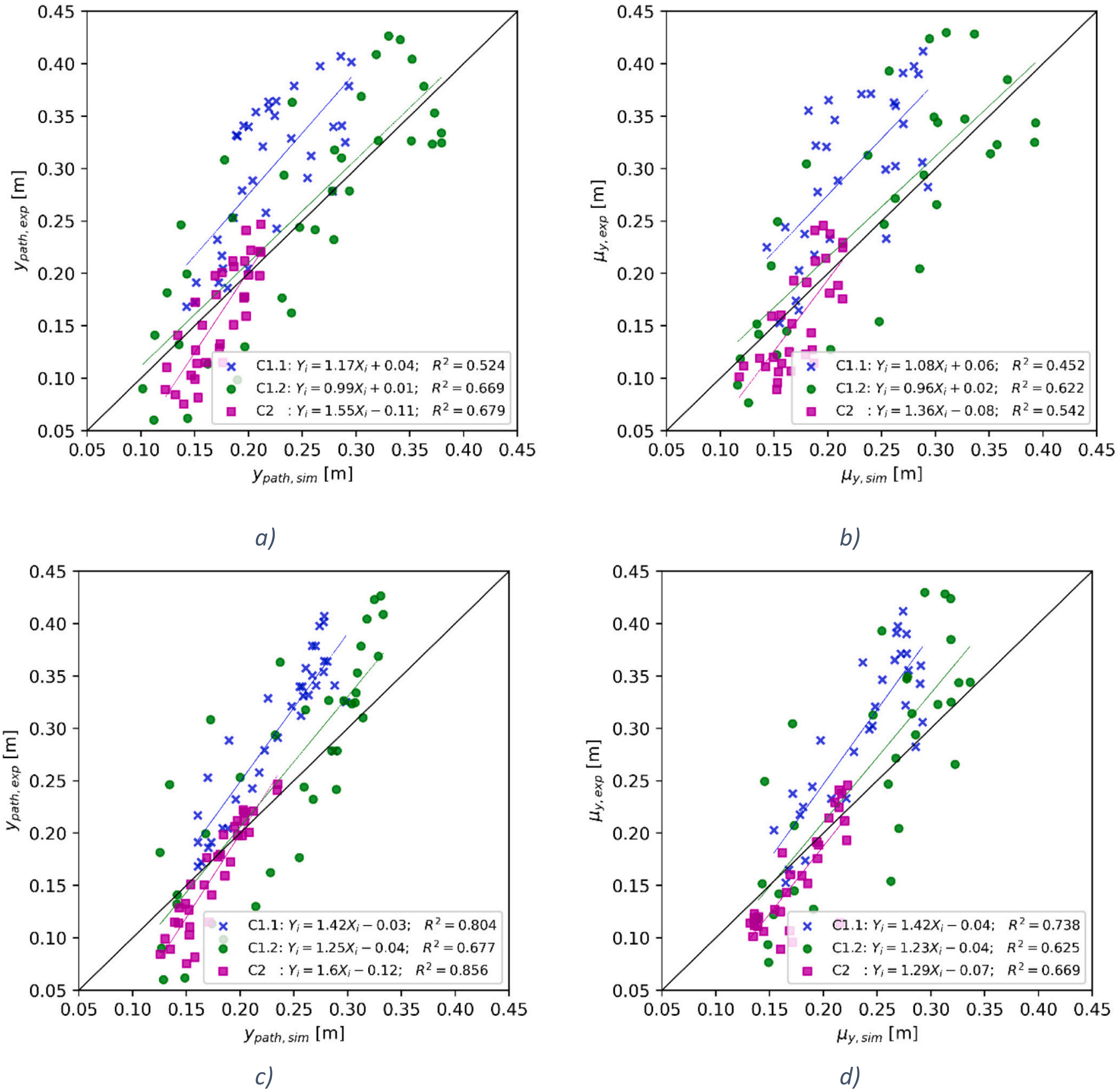

a) b) c) d)

Fig. 7. Experimental and simulated pathline statistics; a) Polynomial regression, y_{path} (without escaping response, B_3); b) Statistical validation, μ_y (without escape response, B_3); c) Polynomial regression, y_{path} (with escape response, B_3); d) Statistical validation, μ_y (with escaping response, B_3).

0.06], [0.96, 1.36], and [0.45, 0.62], respectively before including the escape response, B_3. With the inclusion of the escape response, B_3, the coefficients are in the ranges of [−0.07, −0.04], [1.29, 1.42], and [0.63, 0.73], respectively. The values of the second moment, σ_y (m), of the agent's position along the y-axis are shown in Table 5. These values refer to the whole sample rather than discrete intervals.

3.3. ELAM predictions

Fig. 8 shows the agent's pathline preference when the escape response, B_3, is applied to high velocity zones (Fig. 8a, Fig. 8c, and Fig. 8e) and when it is not (Fig. 8b, Fig. 8d, and Fig. 8f). It is observed that in most cases the carps swimming corridor is reproduced by the agent's upstream migration corridor. C1.1 shows the greatest bias, while C2 shows the most accurate simulation.

3.4. Behavioral energy cost

Fig. 9 shows the spatial distributions of the different agent's behaviors, while Fig. 10 shows the occurrence of each behavior for each case. Overall, the escape response, B_3, is the one with the highest occurrence rate, representing 43%, 53% and 68% of the occurrence for C1.1, C1.2 and C2, respectively. In the cases C1.1 and C1.2, simulation results show that the agent triggers the escape response, B_3, mostly in the baffle sections in which the velocity magnitude is higher**.** In the case C2 instead, the escape response, B_3, has the highest occurrence rate and occurs mostly along the main flow where higher velocities are located. Attraction behavior, B_1, was the second most frequent type of behavior, with occurrence rates of 46%, 30% and 26%, in C1.1, C1.2 and C2, respectively. Attraction behavior, B_1, was primarily located at the transitions from one pool to another or in proximity of the baffles in case C2, whereas it was spread over the pools in cases C1.1 and C1.2. It is further observed that the escape response, B_3, and attraction behavior, B_1, do not appear to follow a clear pattern in cases C1.1 and C1.2. In contrast, the location of these behaviors is more predictable in case C2. Lastly, wall avoidance, B_2, representing wall collision avoidance, is the least frequent, with occurrence rates of 11%, 18% and 9% in C1.1, C1.2 and C2, respectively. Almost all the points where this behavior was triggered are located in proximity of the baffles.

In almost all the domain and in all configurations, the probability P was found to be over 0.05. In fact, 98%, 94% and 90% of total domain are characterized by P values over 0.15 in C1.1, C1.2 and C2, respectively. In addition, after exiting the fifth pool, the agent experiences P values in the range 0.2–0.25. Therefore, pure random walk behavior was not triggered in any of the simulations. Fig. 11 shows the relation between the simulated energy consumption and residence time with and without the escape response, B_3.

Despite the high occurrence of the escape response, B_3, the energy cost increases only by 30.1% on average by adding it in C2. Conversely, in the C1.1 and C1.2 configurations the total energy cost increases by 56.63% and 59.85%, respectively, with a lower occurrence of the escape behavior. The average residence time in the C2 case before including the escape response, B_3,is 14.71 s, and 12.30 s after including it. In C1.1, the residence time is 15.94 s and 13.20 s before and after including the escape response, B_3, respectively, whereas for C1.2, the residence times are respectively 15.09 s and 11.10 s. The residence time decreases by 4 s in C1.2 when the escape response, B_3, is added, while it decreases by 2.7 and 2.4 s in cases C1.1 and C2, respectively.

Table 5
Variance of the carps' transverse position, σ_y, predicted by the ELAM with and without Behavior 3: Escape from high velocity regions.

Case	$\sigma_{y,exp}$ (m)	$\sigma_{y,sim}$ (m)	
		No escaping response, B_3	Escaping response, B_3
C1.1	0.069	0.054	0.065
C1.2	0.059	0.033	0.067
C2	0.055	0.029	0.054

4. Discussion

When designing vertical slot fishways, flow velocities and flow patterns are key features to be considered (Baki and Azimi, 2021). Sanagiotto et al. (2019) mentioned three favorable conditions for an efficient VSF design. First, fish can choose the depth at the slot when swimming from pool to pool. Second, within each pool area, there should be a large resting zone in which the velocity U is much lower than in the main jet and TKE is much lower than in the transition zones between pools. In C1.1 and C1.2 it is observed that high velocity, U, turbulent kinetic energy, TKE, and strain rate, SR, are not concentrated in specific zones, which implies that there are no well-defined resting zones for fish. This is in contrast with the C2 geometry where U, TKE and SR are not randomly distributed in each pool. High TKE zones (>0.035) are located near the baffles and increase in magnitude at each baffle downstream. They are distributed along the jet zone for C1.1 and for C1.2, whereas high TKE zones surround the main jet zone in C2. Third, the main jet, characterized by relatively high velocities, should be clearly defined to avoid disorientation in both upstream and downstream migration (Larinier, 2002). According to the results, C1.1 and C1.2 do not have a clearly defined jet, which might lead to disorientation of the carps and higher spreading of the agent's trajectories in the ELAM simulations (Fig. 8). In contrast, the main jet in C2 is clearly defined by the high velocity magnitude and TKE. Therefore, the path followed by the fish is more predictable in C2 than in C1.

Conversely, flow in the C1.2 case does not exhibit a continuous high-velocity corridor. Zhu et al. (2020) observed this flow pattern in C2 and concluded that this is mainly due to random characteristics of the flow field. Fig. 6 and Fig. 5 show that in the C2 case there is a clear stable jet zone with low strain rate values where the highest velocities are located, whereas in C1.1 and C1.2 this path is not well defined. High values of the velocity strain rate (>10 s^{-1}) are mainly located in the pools in the C1 configuration, and mainly near the walls and baffles in the C2 case. This variable is an indicator of non-uniformity, as higher values imply higher velocity gradients. In this context, the flow is more uniform in C2 than in C1.1 and C1.2.

In the CFD simulations, all hydrodynamic variables are found to be in the range for normal functioning of a VSF. Newbold et al. (2016) measured 0.37–0.78 m/s for U_{crit} and 0.30–1.23 m/s for U_{burst} on their experiments with adult bighead carps. In the same line, Tan et al. (2021) measured around 0.5 m/s for juveniles silver and bighead carps. According to these ranges of values all configurations considered in this work are suitable for a fishway. However, Tan et al. (2018, 2019) reported passage efficiencies of 69.7% and 54.2% for trials in the configurations C1 and C2, respectively. The calibrated coefficients reported in Table 4 agree with the conclusions of Tan et al. (2019), who observed that the velocity strain rate (SR) is not significant for carps' path selection. On the other hand, for C2, the weightings W_j of TKE, U and SR were 0.74, 0.10, and 0.16, respectively. These coefficients are in contrast with those presented by Tan et al. (2018), who found similar influence, W_j, of TKE and U with 0.412 and 0.319, respectively.

Analysis of the TKE values shows that 25.66%, 35.04% and 7.90% of the domain has TKE values above the mean value, μ_{TKE}, in C1.1, C1.2, and C2, respectively. It is observed that in the C2 configuration, TKE values higher than those considered comfortable for the carp are significantly lower than in C1.1 and C1.2. Thus, considering that fish often react negatively to high values of turbulent intensity (Lacey et al., 2012; Silva et al., 2012, 2020), C2 offers a proper condition for passage of Asian carps rather than C1.1 and C1.2, which display higher turbulence intensities. When adding the standard deviation, $\mu_{TKE} \pm \sigma_{TKE}$, the suitable domain increases to 35.82%, 41.36% and 26.01%. As it can be observed from Fig. 4a, carps avoid most of the high turbulent zones in

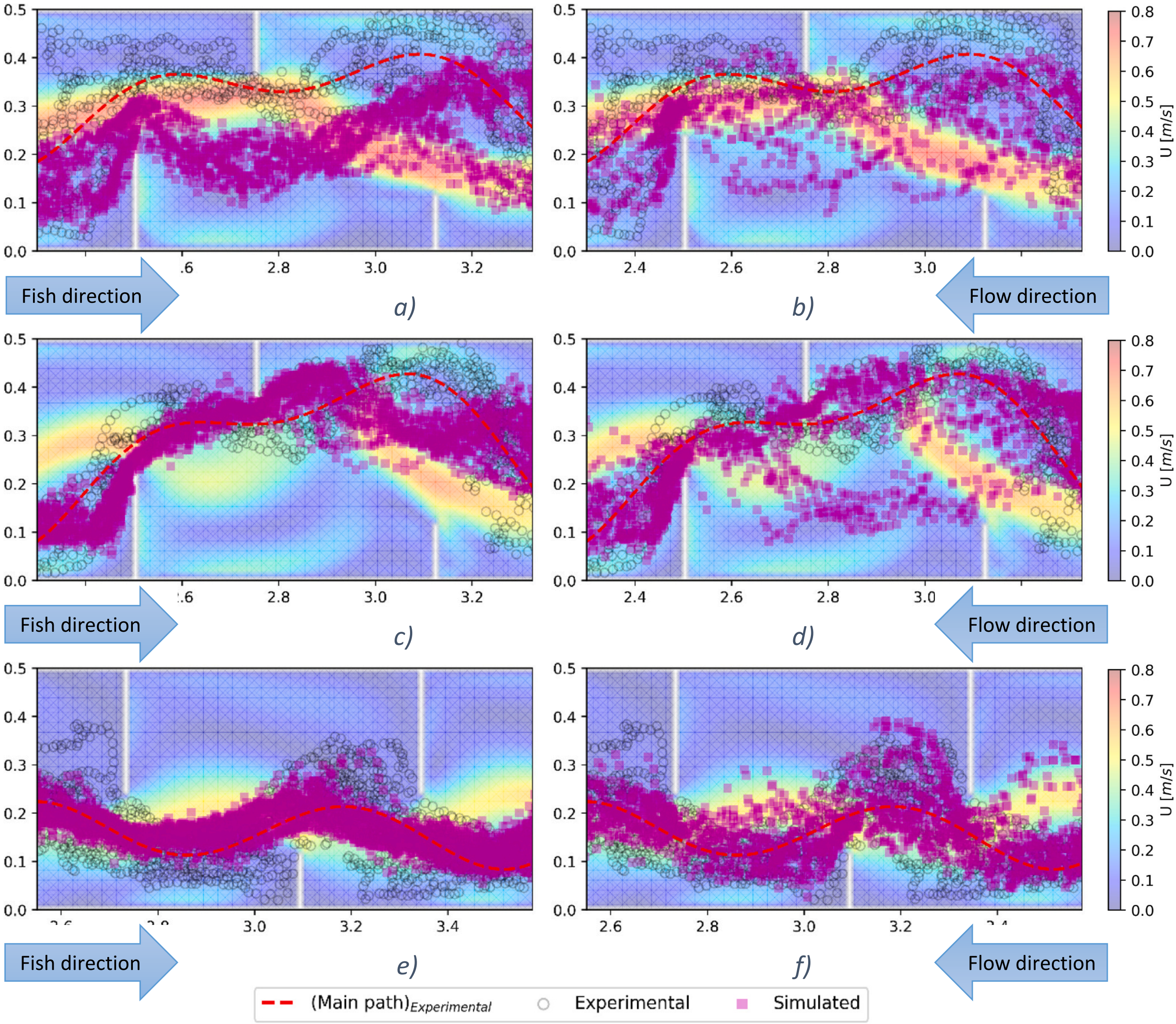

Fig. 8. Simulated carp trajectories a) C1.1; b) C1.1 (Escape response, B_3); c) C1.2; d) C1.2 (Escape response, B_3); e) C2; f) C2 (Escape response, B_3). Red dashed line is the main path obtained through a polynomial regression of the experimental data from Tan et al. (2018, 2019). (For interpretation of the references to colour in this figure legend, the reader is referred to the web version of this article.)

C1.1. In the C1.2 case, instead, fish transits over high turbulent zones and low velocity fields (Fig. 4b). In the case of C2, high values of TKE constrain the carp's upstream migration corridor. We can therefore conclude that TKE is the main driver of the attraction behavior, B_1. These results agree with the observations of Silva et al. (2012) who concluded that the upstream migration of adult Iberian barbels (*Luciobarbus bocagei*) through a pool-type fishway was more influenced by the Reynolds shear stress than the flow velocity. In addition, Silva et al. (2020) observed that smolts of Atlantic salmon (*Salmo salar*) deviated from the main flow direction where TKE was the highest.

The ELAM simulations with B_0, B_1 and B_2 only, displayed good agreement with the experimental tests performed by Tan et al. (2018, 2019), as shown in Fig. 8. Values shown in Figs. 7a and7b are in good agreement with the simulated carp trajectories and the experimental data, but spatial dispersion of the trajectories (Table 5) is not well represented and the values of the coefficient of determination, R^2, are relatively low. The escape response to high velocities, B_3, was therefore added to the IBM. In all the cases the coefficient of determination, R^2, increases, and therefore the correlation between experimental and simulated data improves. Nevertheless, cases C1.1 and C2 display a more significant improvement than C1.2. This can be observed in Fig. 8 which shows that in in the null hypothesis testing, the intercept, a, remains in the same ranges, and the slope, m, increases just slightly for most cases. It can therefore be concluded that the escape response, B_3, slightly improves the predictions in C1.1, slightly decreases the accuracy in the C1.2 case, and significantly improves predictions in C2. In all cases, the correlation, R^2, was significantly better when including Behavior 3. Finally, for the validation based on the second statistical moment, σ_y, Table 5 shows that the inclusion of the escape response, B_3, noticeably improves the prediction of the pathline variability.

When uncertainty is added to the attraction behavior, B_1, by allowing the fish to randomly select among 50% of the most suitable cells, the model successfully predicts the main pathline of experimental data. However, the dispersion of the experimental pathlines is not well reproduced (Table 5). By adding the escape response, B_3, and increasing the uncertainty of cell selection to 75% of the most suitable cells, the ELAM successfully meets all the validation criteria, reproducing both the main migration corridor and the dispersion of the experimental data. As

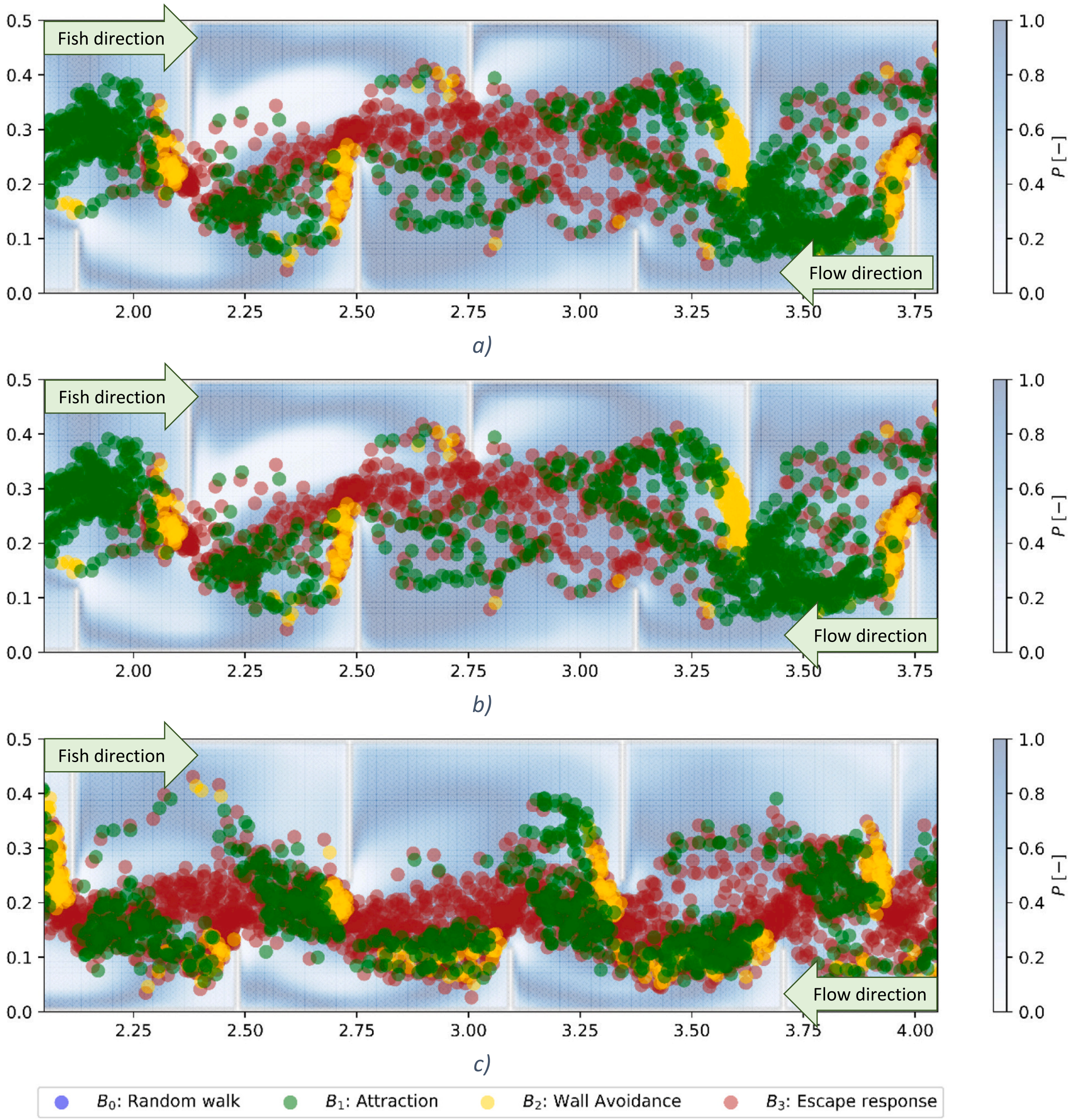

Fig. 9. Spatial distribution of agent behaviors triggered in ELAM simulations for the three test cases a) C1.1; b) C1.2; c) C2. P is the joint probability or the likelihood of the path to be chosen by the agent.

suggested by Zhu et al. (2020), the randomness of the fish trajectories might be related to the randomness of flow characteristics rather than the natural randomness of decision making.

Considering that the flow is more uniform in C2 due to its baffle configuration, and that the agents choose low SR (i.e., more uniform) zones over low velocity zones (Table 3), carps are more exposed to high velocity magnitudes along the mean pathline in C2 than in configurations C1.1 and C1.2. Within the pools 2, 3 and 4, the portions of area containing U values greater than or equal to $\mu_U + 1.75 \bullet \sigma_U$ are respectively 1.32%, 4.48% and 0.49% for C1.1, C1.2 and C2. Considering that Behavior 3 is the most frequent behavior (Fig. 10), it can be concluded that in the simulations the agents tend to swim to zones where the velocities are highest but less variable. It has indeed been observed that, in spite of the high energy expenditure (Webb, 1975), high water velocities attract fish and enhance fish passage (Williams et al., 2012). Moreover, fish choose habitats based not only on the mean hydrodynamic variables but also on their degree of variation (Liao, 2007), with a preference for zones characterized by small gradients. Consistently with this behavior, Fig. 6 shows very low SR values but the highest velocities. This is more noticeable in C2, which displays the most uniform flow of all the cases evaluated. In cases C1.1 and C1.2, the strain rate has no or little influence on path selection. Therefore, the carp pathline is strictly related to turbulent kinetic energy and velocity magnitude.

In our study, we considered both bighead carps and silver carps as Asian carps as if they shared the same behavioral rules and the same range of fish swimming performance indicators. Nevertheless, differences between both species are marked. Hoover et al. (2017) observed that adult bighead carps have more endurance decline than silver carps in counter current swimming. In the same study, juvenile silver carps exhibited higher swimming performance than bighead carps.

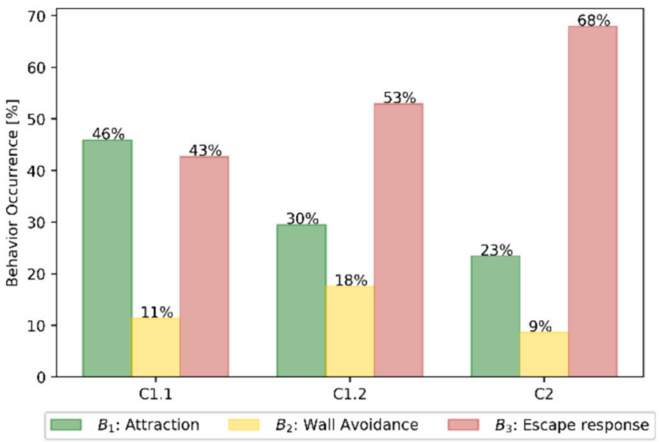

Fig. 10. Frequency of occurrence for each behavior.

Considering that the hydraulics of the VSF are not demanding as the other designs, the ranges used, typically for adults, are consistent with the ELAM predictions. Finally, Fig. 7 and Fig. 8 show that C2 predictions are in better agreement with the experimental results. C2 displays more uniform hydraulics and different fish species than C1.1 and C1.2. Due to constraints in the data published by Tan et al. (2018, 2019), configuration 2, C2, could not be tested with bighead carp. Therefore, it is unclear if the better agreement found in this study is due to the hydraulics or the best fit of silver carp to the behavioral rules.

In summary, in all configurations, the turbulent kinetic energy, TKE, is the main driver of agent's behavior. When baffles are arranged uniformly, the strain rate, SR, is more influential than the velocity magnitude, while the opposite occurs when they are staggered. This confirms that uniformity and flow variability play an important role in the agent's response. A uniform design should therefore be preferred over a staggered arrangement to avoid flow non-uniformity and local variations. Newbold et al. (2016) suggested considering carp's burst swimming speed, U_{burst}, in the design of fishways and its impact on fish energy consumption. When this was considered in the model, good agreement was found between the model results and the experimental data. Finally, energy expenditure per unit time is higher in cases C1.1 and C1.2, for which the escape response, B_3, is not as frequent as in C2. This might be due to velocity magnitudes in C1.1 and C1.2 being considerably higher than in C2, as the energy cost is not only dependent on the agent's velocity. The implementation of the escape response has a significant impact on the energy cost and the residence time in case C1.2. A similar impact on the energy cost is found in C1.1, whereas the residence time is affected only to a minor extent. The energy cost increases just slightly when the escape response, B_3, is considered in case C2, whilst the residence time slightly decreases.

5. Conclusions

The main aim of this study was to evaluate the performance of a Eulerian-Lagrangian model (ELAM) of fish motion in the prediction of fish upstream swimming corridors in VSFs. The proposed model extends the ELAM proposed by Tan et al. (2018) by taking into account the tendency of the fish to avoid collisions with the walls and to escape regions with high flow velocities. The model uses two fish swimming performance indicators, i.e., the critical swimming speed, U_{crit}, and burst swimming speed, U_{burst}, which are characteristic parameters of a fish species. The model adds stochasticity and uncertainty to the fish velocity magnitude and travel direction to address variability due to external and internal, uncorrelated, factors which are not explicitly represented in the model. Three behaviors were initially considered in the ELAM: random walk (B_0), flow attraction (B_1) and wall avoidance (B_2). The model was implemented and tested for a vertical slot fishway with two different geometries under three different hydraulic conditions. The ELAM was found to effectively reproduce the main swimming trajectory of Asian carps through the VSFs, but the predicted dispersion of the pathlines was not accurate. Subsequently, the randomness in the selection of the most suitable cells was increased in high velocity regions, and the radius of the sensory query sphere was reduced. This behavior (B_3) not only increased correlation between experimental and simulated values, but also well reproduced the dispersion of the data. A better representation of the distribution of trajectories along the VSF can provide designers with insights about critical zones in which improvement is needed.

Although the model successfully reproduces carps' migration pathlines, there are some limitations that might need to be addressed in future research. First, the Eulerian input, as in the original model by Tan et al. (2018), is static. The inherent transient nature of the flow field has been proven to affect carps behavior (Zhu et al., 2020). Therefore, it would be useful to investigate model performance with unsteady, turbulent-resolving flow simulations. Second, the Lagrangian framework considers carps as particles. Thus, if the model is used to reproduce adults, which can grow up to 1.2 m of body length (Nico et al., 2023a, 2023b), the mutual interactions between the flow and the fish should be modelled both ways. Finally, since the flow regime of the VSF is subcritical throughout the fishway, juveniles will likely not use the highest values from U_{crit} and U_{burst}. Application of the ELAM to different VSF designs with higher water drops and smaller slots is therefore needed to better understand the range of validity of the model parameters and rules presented in this study.

In conclusion, the evaluation of the fish swimming performance through the estimation of the fish energy consumption can help improve

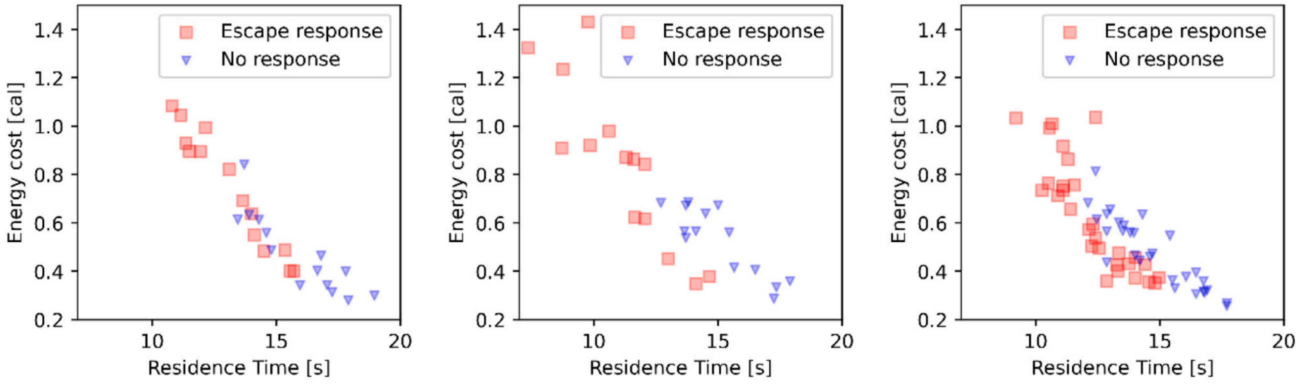

a) b) c)

Fig. 11. Energy consumption vs residence time for cases a) C1.1; b) C1.2; c) C2.

the design of fishways. However, whilst the model presented in this work evaluates both cumulative energy cost and residence time, the predictions of these two variables could not be validated due to limitations in the data available. An additional limitation of the model is that the possibility of the fish taking a rest along the fishway was not considered. Further work is therefore needed to understand fish's energy expenditure and resting behavior. Model testing also needs to be extended to more sophisticated fishway configurations with bigger heads between pools and more complex geometry, and to the case of more exploratory fish species such as salmonids.

Credit authorship contribution statement

M.X. Ruiz-Coello: Writing – review & editing, Writing – original draft, Visualization, Validation, Software, Methodology, Investigation, Formal analysis, Data curation, Conceptualization. **A. Bottacin-Busolin:** Writing – review & editing, Supervision, Conceptualization. **A. Marion:** Writing – review & editing, Supervision, Resources, Project administration, Funding acquisition.

Declaration of competing interest

The authors declare that they have no known competing financial interests or personal relationships that could have appeared to influence the work reported in this paper.

Data availability

Data will be made available on request.

Acknowledgments

This study was performed under the project “RIver flow regulation, fish BEhavior and Status (RIBES) framework”. The project has received funding from the European Union Horizon 2020 Research and Innovation Programme under the Marie Sklodowska-Curie Actions, Grant Agreement No. 860800.

References

An, R., Li, J., Liang, R., Tuo, Y., 2016. Three-dimensional simulation and experimental study for optimising a vertical slot fishway. J. Hydro-Environ. Res. 12, 119–129. https://doi.org/10.1016/j.jher.2016.05.005.

Baharvand, S., Lashkar-Ara, B., 2021. Hydraulic design criteria of the modified meander C-type fishway using the combined experimental and CFD models. Ecol. Eng. 164, 106207 https://doi.org/10.1016/j.ecoleng.2021.106207.

Baharvand, S., Ahmari, H., Taghvaei, P., 2023. Developing a Lagrangian sediment transport model for open channel flows. Int. J. Sediment Res. 38, 153–165. https://doi.org/10.1016/j.ijsrc.2022.09.003.

Baki, A.B.M., Azimi, A.H., 2021. Hydraulics and design of fishways II: vertical-slot and rock-weir fishways. J. Ecohydraul. 0, 1–13. https://doi.org/10.1080/24705357.2021.1981780.

Barton, A., Keller, R., 2003. 3D free surface model of a vertical slot fishway. In: Proceedings of the XXX IAHR Congress. Thesaloniki, Grece.

Bombač, M., Novak, G., Rodič, P., Matjaž, Č., 2014. Numerical and physical model study of a vertical slot fishway. J. Hydrol. Hydromech. 62, 150–159. https://doi.org/10.2478/johh-2014-0013.

Bunt, C.M., Castro-Santos, T., Haro, A., 2012. Performance of Fish Passage Structures at Upstream Barriers to Migration. River Res. Appl. 28, 457–478. https://doi.org/10.1002/rra.1565.

Cai, L., Chen, J., Johnson, D., Tu, Z., Huang, Y., 2020. Effect of body length on swimming capability and vertical slot fishway design. Glob. Ecol. Conserv. 22, e00990 https://doi.org/10.1016/j.gecco.2020.e00990.

Castro-Santos, T., 2005. Optimal swim speeds for traversing velocity barriers: an analysis of volitional high-speed swimming behavior of migratory fishes. J. Exp. Biol. 208, 421–432. https://doi.org/10.1242/jeb.01380.

Cea, L., Pena, L., Puertas, J., Vázquez-Cendón, M.E., Peña, E., 2007. Application of several depth-averaged turbulence models to simulate flow in vertical slot fishways. J. Hydraul. Eng. 133, 160–172. https://doi.org/10.1061/(ASCE)0733-9429(2007)133:2(160).

Codling, E.A., Plank, M.J., Benhamou, S., 2008. Random walk models in biology. J. R. Soc. Interface 5, 813–834. https://doi.org/10.1098/rsif.2008.0014.

Correndo, A.A., Hefley, T.J., Holzworth, D.P., Ciampitti, I.A., 2021. Revisiting linear regression to test agreement in continuous predicted-observed datasets. Agric. Syst. 192, 103194 https://doi.org/10.1016/j.agsy.2021.103194.

DeAngelis, D.L., Grimm, V., 2014. Individual-based models in ecology after four decades. F1000Prime Rep. 6, 39. https://doi.org/10.12703/P6-39.

ESI Group, 2022. Overview OpenFOAM [WWW Document]. URL https://www.openfoam.com/documentation/overview (accessed 12.20.21).

Fang, K., Sivakumar, B., Woldemeskel, F.M., Jothiprakash, V., 2019. Streamflow connectivity in a large-scale River Basin. In: Singh, S.K., Dhanya, C.T. (Eds.), Hydrology in a Changing World: Challenges in Modeling. Springer Water. Springer International Publishing, Cham, pp. 205–223. https://doi.org/10.1007/978-3-030-02197-9_10.

Fang, D., Zhou, Y., Ren, P., Peng, Y., Xue, X., Ren, L., Xu, D., 2022. The status of silver carp resources and their complementary mechanism in the Yangtze River. Front. Mar. Sci. 8.

Feng, H., Wang, Z., Todd, P.A., Lee, H.P., 2019. Simulations of self-propelled anguilliform swimming using the immersed boundary method in OpenFOAM. Eng. Appl. Comput. Fluid Mech. 13, 438–452. https://doi.org/10.1080/19942060.2019.1609582.

Fish, F.E., 2010. Swimming strategies for energy economy. In: Fish Locomotion. CRC Press.

Fuentes-Pérez, J.F., García-Vega, A., Sanz-Ronda, F.J., de Paredes, A.M.A., 2017. Villemonte's approach: a general method for modeling uniform and non-uniform performance in stepped fishways. Knowl. Manag. Aquat. Ecosyst. 23 https://doi.org/10.1051/kmae/2017013.

Fuentes-Pérez, J.F., Silva, A.T., Tuhtan, J.A., García-Vega, A., Carbonell-Baeza, R., Musall, M., Kruusmaa, M., 2018. 3D modelling of non-uniform and turbulent flow in vertical slot fishways. Environ. Model. Softw. 99, 156–169. https://doi.org/10.1016/j.envsoft.2017.09.011.

Fuentes-Pérez, J.F., Quaresma, A.L., Pinheiro, A., Sanz-Ronda, F.J., 2022. OpenFOAM vs FLOW-3D: a comparative study of vertical slot fishway modelling. Ecol. Eng. 174, 106446 https://doi.org/10.1016/j.ecoleng.2021.106446.

Gao, Z., Andersson, H.I., Dai, H., Jiang, F., Zhao, L., 2016. A new Eulerian–Lagrangian agent method to model fish paths in a vertical slot fishway. Ecol. Eng. 88, 217–225. https://doi.org/10.1016/j.ecoleng.2015.12.038.

George, A.E., Chapman, D.C., 2013. Aspects of embryonic and larval development in bighead carp hypophthalmichthys nobilis and silver carp hypophthalmichthys molitrix. PLoS One 8, e73829. https://doi.org/10.1371/journal.pone.0073829.

Goodwin, R.A., Nestler, J.M., Anderson, J.J., Weber, L.J., Loucks, D.P., 2006. Forecasting 3-D fish movement behavior using a Eulerian–Lagrangian–agent method (ELAM). Ecol. Model. 192, 197–223. https://doi.org/10.1016/j.ecolmodel.2005.08.004.

Goodwin, R.A., Politano, M., Garvin, J.W., Nestler, J.M., Hay, D., Anderson, J.J., Weber, L.J., Dimperio, E., Smith, D.L., Timko, M., 2014. Fish navigation of large dams emerges from their modulation of flow field experience. Proc. Natl. Acad. Sci. 111, 5277–5282. https://doi.org/10.1073/pnas.1311874111.

Grill, G., Lehner, B., Thieme, M., Geenen, B., Tickner, D., Antonelli, F., Babu, S., Borrelli, P., Cheng, L., Crochetiere, H., Ehalt Macedo, H., Filgueiras, R., Goichot, M., Higgins, J., Hogan, Z., Lip, B., McClain, M.E., Meng, J., Mulligan, M., Nilsson, C., Olden, J.D., Opperman, J.J., Petry, P., Reidy Liermann, C., Sáenz, L., Salinas-Rodríguez, S., Schelle, P., Schmitt, R.J.P., Snider, J., Tan, F., Tockner, K., Valdujo, P. H., van Soesbergen, A., Zarfl, C., 2019. Mapping the world's free-flowing rivers. Nature 569, 215–221. https://doi.org/10.1038/s41586-019-1111-9.

Hammer, C., 1995. Fatigue and exercise tests with fish. Comp. Biochem. Physiol. A Physiol. 112, 1–20. https://doi.org/10.1016/0300-9629(95)00060-K.

Hermoso, V., Filipe, A.F., 2021. Offsetting connectivity loss in rivers: Towards a no-net-loss approach for barrier planning. Biol. Conserv. 256, 109043 https://doi.org/10.1016/j.biocon.2021.109043.

Hirt, C.W., Nichols, B.D., 1981. Volume of fluid (VOF) method for the dynamics of free boundaries. J. Comput. Phys. 39, 201–225. https://doi.org/10.1016/0021-9991(81)90145-5.

Hoover, J.J., Zielinski, D.P., Sorensen, P.W., 2017. Swimming performance of adult bighead carp Hypophthalmichthys nobilis (Richardson, 1845) and silver carp H. molitrix (Valenciennes, 1844). J. Appl. Ichthyol. 33, 54–62. https://doi.org/10.1111/jai.13199.

Jiang, L., Diao, M., Sun, H., Ren, Y., 2018. Numerical modeling of flow over a rectangular broad-crested weir with a sloped upstream face. Water 10, 1663. https://doi.org/10.3390/w10111663.

Kemp, P.S., Anderson, J.J., Vowles, A.S., 2012. Quantifying behaviour of migratory fish: Application of signal detection theory to fisheries engineering. Ecol. Eng. 41, 22–31. https://doi.org/10.1016/j.ecoleng.2011.12.013.

Kulić, T., Lončar, G., Kovačević, M., Fliszar, R., 2021. Application of agent-based modelling for selecting configuration of vertical slot fishway. Građevinar 73. https://doi.org/10.14256/JCE.3150.2021.

Lacey, R.W.J., Neary, V.S., Liao, J.C., Enders, E.C., Tritico, H.M., 2012. The ipos framework: linking fish swimming performance in altered flows from laboratory experiments to rivers. River Res. Appl. 28, 429–443. https://doi.org/10.1002/rra.1584.

Larinier, M., 1992. Passes à bassins successifs, prébarrages et rivières artificielles. Bull. Fr. Pêche Piscic. 45–72 https://doi.org/10.1051/kmae:1992005.

Larinier, M., 2002. Pool fishways, pre-barrages and natural bypass channels. Bull. Fr. Pêche Piscic. 54–82 https://doi.org/10.1051/kmae/2002108.

Liao, J.C., 2007. A review of fish swimming mechanics and behaviour in altered flows. Philos. Trans. Biol. Sci. 362, 1973–1993.

Lucas, M.C., Baras, E., 2001. Migration or Fresh Water Fishes. Blackwell Science, Oxford, UK.

McHenry, M.J., Liao, J.C., 2014. The hydrodynamics of flow stimuli. In: Coombs, S., Bleckmann, H., Fay, R.R., Popper, A.N. (Eds.), The Lateral Line System. Springer Handbook of Auditory Research. Springer, New York, NY, pp. 73–98. https://doi.org/10.1007/2506_2013_13.

McIntyre, P.B., Reidy Liermann, C., Childress, E., Hamann, E.J., Hogan, J., Januchowski-Hartley, S., Koning, A.A., Neeson, T., Oele, D., Pracheil, B.M., 2016. Conservation of migratory fishes in freshwater ecosystems. In: Conservation of Freshwater Fishes. Cambridge University Pres, Cambridge,UK.

Montgomery, J., Carton, G., Voigt, R., Baker, C., Diebel, C., 2000. Sensory processing of water currents by fishes. Philos. Trans. Biol. Sci. 355, 1325–1327.

Muhawenimana, V., Wilson, C., Ouro, P., Cable, J., 2019. Spanwise cylinder wake hydrodynamics and fish behavior. Water Resour. Res. 55, 8569–8582. https://doi.org/10.1029/2018WR024217.

Nestler, J.M., Stewardson, M.J., Gilvear, D.J., Webb, J.A., Smith, D.L., 2016. Ecohydraulics exemplifies the emerging “paradigm of the interdisciplines.”. J. Ecohydraul. 1, 5–15. https://doi.org/10.1080/24705357.2016.1229142.

Newbold, L.R., Shi, X., Hou, Y., Han, D., Kemp, P.S., 2016. Swimming performance and behaviour of bighead carp (Hypophthalmichthys nobilis): Application to fish passage and exclusion criteria. Ecol. Eng. 95, 690–698. https://doi.org/10.1016/j.ecoleng.2016.06.119.

Nico, L., Fuller, P., Baker, E., Narlock, C., Nunez, G., Sturtevant, R., Alsip, P., Redinger, J., 2023a. *Hypophthalmichthys nobilis* (Richardson, 1845): U.S. Geological Survey, Nonindigenous Aquatic Species Database, Gainesville, FL.

Nico, L., Nunez, G., Baker E., Alsip, P., Redinger, J., 2023b. *Hypophthalmichthys molitrix* (Valenciennes in Cuvier and Valenciennes, 1844): U.S. Geological Survey, Nonindigenous Aquatic Species Database, Gainesville, FL.

Nilsson, C., Reidy, C.A., Dynesius, M., Revenga, C., 2005. Fragmentation and Flow Regulation of the World’s large River Systems. Science 308, 405–408. https://doi.org/10.1126/science.1107887.

Noonan, M.J., Grant, J.W.A., Jackson, C.D., 2012. A quantitative assessment of fish passage efficiency. Fish Fish. 13, 450–464. https://doi.org/10.1111/j.1467-2979.2011.00445.x.

Periáñez, R., 2020. A Lagrangian oil spill transport model for the Red Sea. Ocean Eng. 217, 107953 https://doi.org/10.1016/j.oceaneng.2020.107953.

Piper, A.T., Manes, C., Siniscalchi, F., Marion, A., Wright, R.M., Kemp, P.S., 2015. Response of seaward-migrating European eel (Anguilla anguilla) to manipulated flow fields. Proc. Biol. Sci. 282, 1–9.

Quaranta, E., Katopodis, C., Comoglio, C., 2019. Effects of bed slope on the flow field of vertical slot fishways. River Res. Appl. 35, 656–668. https://doi.org/10.1002/rra.3428.

Railsback, S.F., Grimm, V., 2012. Agent-Based and Individual-Based Modeling: A Practical Introduction, 1st ed. Princeton University Press, Oxfordshire, UK.

Rajaratnam, N., Van der Vinne, G., Katopodis, C., 1986. Hydraulics of Vertical Slot Fishways. J. Hydraul. Eng. 112, 909–927. https://doi.org/10.1061/(ASCE)0733-9429(1986)112:10(909).

Rajaratnam, N., Katopodis, C., Solanki, S., 1992. New designs for vertical slot fishways. Can. J. Civ. Eng. https://doi.org/10.1139/l92-049.

Ruiz-Coello, M.R., Sandoval, R., Bottacin-Busolin, A., Guerra, M.J., Rios, L., Ortega, P., Marion, A., 2024. Numerical approaches to evaluate the hydraulics of Vertical Slot Fishways: A comparative study of 2D and 3D simulations. In: GeoPlanet: Earth and Planetary Sciences; Environmental Eydraulics. Presented at the 40th International School of Hydraulics: Advances in Hydraulic Research. Springe Link, Gdansk, Poland (https://doi.org/10.1007/978-3-031-56093-4_26 [In Press, SubID: 8398160344).

Sanagiotto, D.G., Rossi, J.B., Bravo, J.M., 2019. Applications of computational fluid dynamics in the design and rehabilitation of nonstandard vertical slot fishways. Water 11, 199. https://doi.org/10.3390/w11020199.

Silva, A.T., Katopodis, C., Santos, J.M., Ferreira, M.T., Pinheiro, A.N., 2012. Cyprinid swimming behaviour in response to turbulent flow. Ecol. Eng. 44, 314–328. https://doi.org/10.1016/j.ecoleng.2012.04.015.

Silva, A.T., Lucas, M.C., Castro-Santos, T., Katopodis, C., Baumgartner, L.J., Thiem, J.D., Aarestrup, K., Pompeu, P.S., O’Brien, G.C., Braun, D.C., Burnett, N.J., Zhu, D.Z., Fjeldstad, H.-P., Forseth, T., Rajaratnam, N., Williams, J.G., Cooke, S.J., 2018. The future of fish passage science, engineering, and practice. Fish Fish. 19, 340–362. https://doi.org/10.1111/faf.12258.

Silva, A.T., Bærum, K.M., Hedger, R.D., Baktoft, H., Fjeldstad, H.-P., Gjelland, K.Ø., Økland, F., Forseth, T., 2020. The effects of hydrodynamics on the three-dimensional downstream migratory movement of Atlantic salmon. Sci. Total Environ. 705, 135773 https://doi.org/10.1016/j.scitotenv.2019.135773.

Smith, E.P., Rose, K.A., 1995. Model goodness-of-fit analysis using regression and related techniques. Ecol. Model. 77, 49–64. https://doi.org/10.1016/0304-3800(93)E0074-D.

Stamou, A.I., Mitsopoulos, G., Rutschmann, P., Bui, M.D., 2018. Verification of a 3D CFD model for vertical slot fish-passes. Environ. Fluid Mech. 18, 1435–1461. https://doi.org/10.1007/s10652-018-9602-z.

Tan, J., Tao, L., Gao, Z., Dai, H., Shi, X., 2018. Modeling fish movement trajectories in relation to hydraulic response relationships in an experimental fishway. Water 10, 1511. https://doi.org/10.3390/w10111511.

Tan, J., Gao, Z., Dai, H., Yang, Z., Shi, X., 2019. Effects of turbulence and velocity on the movement behaviour of bighead carp (Hypophthalmichthys nobilis) in an experimental vertical slot fishway. Ecol. Eng. 127, 363–374. https://doi.org/10.1016/j.ecoleng.2018.12.002.

Tan, J., Li, H., Guo, W., Tan, H., Ke, S., Wang, J., Shi, X., 2021. Swimming performance of four carps on the Yangtze River for fish passage design. Sustainability 13, 1575. https://doi.org/10.3390/su13031575.

Tan, J., Liu, Z., Wang, Yu, Wang, Yuanyang, Ke, S., Shi, X., 2022. Analysis of movements and behavior of bighead carps (Hypophthalmichthys nobilis) considering fish passage energetics in an experimental vertical slot fishway. Animals 12, 1725. https://doi.org/10.3390/ani12131725.

Tritico, H.M., Cotel, A.J., 2010. The effects of turbulent eddies on the stability and critical swimming speed of creek chub (Semotilus atromaculatus). J. Exp. Biol. 213, 2284–2293. https://doi.org/10.1242/jeb.041806.

van Netten, S.M., McHenry, M.J., 2014. The biophysics of the fish lateral line. In: Coombs, S., Bleckmann, H., Fay, R.R., Popper, A.N. (Eds.), The Lateral Line System. Springer Handbook of Auditory Research. Springer, New York, NY, pp. 99–119. https://doi.org/10.1007/2506_2013_14.

Webb, P.W., 1975. Hydrodynamics and energetics of fish propulsion, Catalogue no. Fs 94–190. ed. Fisheries and Marine Service Department of the Environmen, Ottawa, Canada.

Williams, J.G., Armstrong, G., Katopodis, C., Larinier, M., Travade, F., 2012. Thinking like a fish: a key ingredient for development of effective fish passage facilities at river obstructions. River Res. Appl. 28, 407–417. https://doi.org/10.1002/rra.1551.

Willis, J., 2011. Modelling swimming aquatic animals in hydrodynamic models. Ecol. Model. 222, 3869–3887. https://doi.org/10.1016/j.ecolmodel.2011.10.004.

Windsor, S.P., Tan, D., Montgomery, J.C., 2008. Swimming kinematics and hydrodynamic imaging in the blind Mexican cave fish (Astyanax fasciatus). J. Exp. Biol. 211, 2950–2959. https://doi.org/10.1242/jeb.020453.

Windsor, S.P., Norris, S.E., Cameron, S.M., Mallinson, G.D., Montgomery, J.C., 2010. The flow fields involved in hydrodynamic imaging by blind Mexican cave fish (Astyanax fasciatus). Part II: gliding parallel to a wall. J. Exp. Biol. 213, 3832–3842. https://doi.org/10.1242/jeb.040790.

Yang, J.M., Yang, J.Y., Liu, S., Hoogenboom, G., 2014. An evaluation of the statistical methods for testing the performance of crop models with observed data. Agric. Syst. 127, 81–89. https://doi.org/10.1016/j.agsy.2014.01.008.

Zhu, G., Zhou, Z., Andersson, H.I., 2020. Role of transient characteristics in fish trajectory modeling. Sustainability 12, 6765. https://doi.org/10.3390/su12176765.